RELATIONSHIP BETWEEN LEAF AREA INDEX (LAI) ESTIMATED BY TERRESTRIAL LIDAR AND REMOTELY SENSED VEGETATION INDICES AS A PROXY TO FOREST CARBON SEQUESTRATION

Nayani Thanuja Ilangakoon

A Thesis

Submitted to the Graduate College of Bowling Green
State University in partial fulfillment of
the requirements for the degree of

MASTER OF SCIENCE

August 2014

Committee:

Peter Gorsevski, Advisor

Anita Simic

Kurt Panter

Jeff Snyder

ABSTRACT

Peter Gorsevski, Advisor

Leaf area index (LAI) is an important indicator of ecosystem conditions and an important key biophysical variable to many ecosystem models. The LAI in this study was measured by Leica ScanStation C 10 Terrestrial Laser Scanner (TLS) and a hand-held Li-Cor LAI-2200 Plant Canopy Analyzer for understanding differences derived from the two sensors. A total of six different LAI estimates were generated using different methods for the comparisons. The results suggested that there was a reasonable agreement (i.e., the correlations $r > 0.50$) considering a total of 30 plots and limited land cover types sampled. The predicted LAI from spectral vegetation indices including WDVI, DVI, NDVI, SAVI, and PVI3 which were derived from Landsat TM imagery were used to identify statistical relationships and for the development of the Bayesian inference model. The Bayesian Linear Regression (BLR) approach was used to scale up LAI estimates and to produce continuous field surfaces for the Oak Openings Region in NW Ohio. The results from the BLR provided details about the parameter uncertainties but also insight about the potential that different LAIs can be used to predict foliage that has been adjusted by removing the wooden biomass with reasonable accuracy. For instance, the modeled residuals associated with the LAI estimates from TLS orthographic projection that consider only foliage had the lowest overall model uncertainty with lowest error and residual dispersion range among the six spatial LAI estimates. The deviation from the mean LAI prediction map derived from the six estimates hinted that sparse and open areas that relate to vegetation structure were associated with the highest error. However, although in many studies TLS has been shown to hold a great potential for quantifying vegetation structure, in this study the quantified relationship

between LAI and the vegetation indices did not yield any statistical relationship that needs to be further explore.

To my loving husband Udaya, parents and to dear friends for their invaluable encouragement, dedication and love.

ACKNOWLEDGMENTS

I gratefully acknowledge my advisor Dr. Peter Gorsevski who gave the great support, encourage, mentorship, and motivation throughout the research as well as last two years of my stay at BGSU. I was lucky enough to study under your supervision where I had greatest opportunity to expose many new fields, software as well as applications. I also grateful to Karen Menard, Research and Monitoring Supervisor, Oak Opening Metro Park, Toledo for giving me permission and support at data collection .The Committee members, Dr. Kurt Panter, Dr. Jeff Snyder, and Dr. Anita Simic are also acknowledged for their support. I also convey my gratitude to the faculty and staff, the Department of Geology, Bowling Green State University.

Finally, I would like to thank my loving parents, husband, brothers and friends. You are my strength, my pride and my belief. Thank you very much for your hand being always with me.

TABLE OF CONTENTS

INTRODUCTION

The ecosystems provide an important carbon sink or artificial reservoir by which atmospheric carbon dioxide taken by plants through photosynthesis is stored as carbon in biomass and soil (Dong et al., 2003; Hashimoto et al., 2012; Houghton, 2005; Patenaude et al., 2004; Turner et al., 2004). The process, known as carbon sequestration helps to offset sources of atmospheric carbon dioxide and could play a critical role in the mitigation of negative effects of climate change. In the United States, forest carbon sinks have been estimated to offset 16 % of total emissions from burning fossil fuels, but continued deforestation from natural and anthropogenic causes undermines future biomass stocks and other important carbon sink functions (USDA-FS, 2013). Thus, quantifying and monitoring carbon stocks is of great interest for assessing forest biomass sinks for carbon sequestration as a part of global, regional, and local mitigation efforts (UN FCCC, n.d.).

Net primary production (NPP) from forest biomass is one of the most important ecological parameters for estimating carbon stocks especially for large spatial scales (Cao and Woodward, 2002; Potter et al., 2011; Running et al., 2004; Turner et al., 2004; Zaehle et al., 2006). NPP is a spatially distributed ecological parameter that represents the difference of carbon stored in a plant from the gross photosynthetic product which is adjusted for autotrophic respiration (i.e., the respiration releases a proportion of the absorbed carbon). NPP is estimated using different models of which the spatially measured leaf area index (LAI) is used as a key biophysical variable (Liu et al., 1999; Reich et al., 1999; Zheng and Moskal, 2009). The LAI is a dimensionless measure of canopy foliage content, defined as the amount of leaf area (m^2) in a canopy per unit ground area (m^2) (Zheng and Moskal, 2012b). This index measures the photosynthetic surface area which is directly proportional to the NPP of a plant species (Davidson, 2002).

There are many attempts to estimate the spatial distribution of LAI using sensor derived spectral responses through various remote sensing applications (Chen et al., 2002; Gamon et al., 1995; Haboudane et al., 2004). These spectral responses are measured in terms of vegetation indices derived from red and near-infrared (NIR) bands. The most profound derivation of LAI is from slope based spectral vegetation indices such as the Normalized Difference Vegetation Index (NDVI), expressed as the difference between the NIR and red bands normalized by the sum of those bands (Turner et al., 1999). The distance based vegetation indices use the perpendicular vegetation index (PVI) concept which aims to eliminate the effect of soil background over surfaces of incomplete vegetation cover. However, spatial variability in soil coverage within an image or satellite data set creates difficulties in their formulation for assessing vegetation cover. Improvements to the PVI have yielded other modified indices referred to as PVI1, PVI2, and PVI3. Further, some indices such as Difference Vegetation Index (DVI) uses the soil line concept, which describes the typical range of soil spectral curve in red and NIR bi-spectral plots (i.e., the soil line is computed by simple regression of NIR against red band measurements for a sample of bare soil pixels) (Baret and Guyot, 1991; Gilabert et al., 2002, Huete, 1988; Kandwal et al., 2009; Richardson and Wiegand, 1977). In addition, indices such as Soil Adjusted Vegetation Index (SAVI) and Weighted Difference Vegetation Index (WDVI) have used ideas to correct for the soil noises which are greatly affected by common weather conditions such as soil moisture (Clever, 1988, Huete, 1988, Richardson and Wiegand, 1977).

Often those indices are calculated from imagery acquired either by multispectral sensors such as MODIS (Running et al., 2004), Landsat TM (Turner et al., 1999) and Landsat ETM+, or by hyperspectral sensors mounted in aircrafts or in satellites such as AVIRIS, CASI (Haboudane et al., 2002; Lee et al., 2004), and Hyperion (Bulcock and Jewitt, 2010). The measured spectral responses are then converted to the LAI through implementation of empirical relationships with the "filed measured LAI." However, the reliability and the accuracy of the LAI estimates depend on the accuracy of "*in situ*" measurements, the effect of land cover heterogeneity associated with the instrument pixel size resolution, the influence of the atmosphere, sensor and light source position, overlapping and clumping of leaves associated with the inclination and azimuth, and the obstruction of canopy components other than leaves (Zhao et al., 2005; Zheng and Moskal, 2009).

The "*in situ*" or field-based LAI quantification methods can be explained either as direct or indirect methods (Asner et al., 2003; Breda, 2003; Chason et al., 1991). The direct LAI measurement methods include destructive tree harvesting and non-destructive litter fall collection (Asner et al., 2003). The vertical (Groeneveld, 1997) and inclined (Jonckheere et al., 2004) point quadrat, and tree allometric relationships (Breda et al. 2003; Mencuccini and Grace, 1995) are some of the contact indirect methods which are used to measure LAI. The non-contact indirect methods of LAI estimation include optical methods. The proportion of light penetrating through a canopy is a function of incident irradiance, canopy structure and species specific optical properties of the canopy. Therefore, in these optical methods, the measured quantities often yield two factors called gap fraction and gap size distribution as a proxy for LAI estimation. For example, Plant Area Index (PAI) (Neumann et al. 1989), Vegetation Area Index (VAI) (Fassnacht et al., 1994), Foliage Area Index (FAI) (Welles and Norman, 1991), or

Effective LAI (L_e) (Chen et al., 1991) are indices measured based on gap fraction as a surrogate of ground based LAI measurements. Such indices do not consider the removal of the effect of stems, branches, and flowers (clumping effect) to the photosynthetically active leaf area (Jonckheere et al., 2004) as well as the influence from zenith and azimuth of both the sun and the leaves (Jonckheere et al., 2004).

Hemispherical photos (Asner et al., 2003; Chen et al., 1991; Jonckheere et al., 2004), and instruments such as LAI-2200 plant canopy analyzer, Demon, Ceptometer, TRAC, and other hybrid instruments such as Multiband Vegetation Imager (MVI) are a few examples that are used to estimate the LAI indirectly through implementation of optical methods (Jonckheere et al., 2004; Zhao et al., 2011). The gap fraction and gap size distribution based optical methods show a wide range of heterogeneity with respect to each other (Chen et al., 1997; Pacheco et al., 2001; Zhao et al., 2005) as well as to the direct tree harvesting or litter fall collection methods (Dewey et al., 2006; Van Gardingen et al., 1999) which are considered as the most accurate methods of LAI quantification (Dufrene and Breda, 1995). In addition, most of these indirect methods show correlations only with the broadleaf forests, and therefore, they are not applicable to the needle leaf forests (Asner et al., 2003; Chen and Chilar, 1995).

More recently, terrestrial laser scanning (TLS), also known as ground-based LiDAR (Light Detection and Ranging) has been used as an alternative indirect method for quantifying aboveground biomass and LAI (Côté, 2009; Hosoi and Omasa, 2007; Lim et al., 2003; Zhao el al., 2005). The data collected by this emerging remote sensing method represents direct measurements of three-dimensional (3-D) distribution of plant canopies at individual tree or stand levels which is difficult and costly to obtain through traditional data collection. The TLS is used for close-range and high-accuracy applications which provide accurate measures of distances to biomass using a large number of sampling laser beams. The laser beam's energy interacts with the biomass and other objects, and reflects a partial amount of the energy while the rest of the energy is lost due to absorption or transmission. The proportion of energy that returns to the scanner represents discrete measurement and intensity values of a point cloud (Hosoi and Omasa, 2006; Kwak et al., 2007; Moaskal and Zheng, 2011; Zheng and Moskal, 2012a; Zhao et al., 2005). The resulted point cloud is a function of different parameters such as the resolving power of individual laser pulses (Van Der Zande et al., 2006), the zenith and azimuth angular resolution of the instrument (Zhao et al., 2005), the maximum resolvable distance of targets (Van Der Zande et al., 2006), sensor position and number of scans per plot (Lovell et al., 2011; Yao et al., 2011; Zheng and Moskal, 2012b), and the canopy structure defined by the homogeneity, heterogeneity, and the species composition (Henning and Radtke, 2006; Zheng and Moskal, 2012b). The main advantage of TLS in LAI estimates is the high accuracy of data cloud measurements that are not influenced by the sun orientation as well as the applicability to broadleaf and needle leaf forest plots at different stand level scales (Chasmer et al., 2006; Huang and Pretzsch, 2010; Zhao et al., 2005; Zheng and Moskal, 2012a).

The field-based measurements are often correlated with satellite observations from Landsat or MODIS to scale up LAI and to produce continuous field surfaces used for NPP estimates. However, these predicted LAI shows different levels of uncertainty that influences the estimates of forest carbon. The uncertainty in predicted quantities of LAI arises from different sources including data collection, processing and analysis of image and ground data, and model development (Foody and Atkinson, 2002). For example, some of the TLS-based uncertainties arise from the complex leaf structure originated by the spatial variability, shadow effect, leaf inclination, and the effect of non-photosynthetic tissues (Hosoi and Omasa , 2007; Jupp et al., 2009; Moskal and Zheng, 2009 ;Van Der Zande et al., 2006). Additional uncertainties are enhanced by other influencing factors such as lack of knowledge about specific parameters, selection of explanatory variables and models, or other factors used for up scaling from finer to courser spatial resolutions (Jupp et al., 2009; Wu & Li, 2006; Zheng and Moskal, 2009; Richardson et al., 2011).

The lack of knowledge about specific LAI estimates and difficulties of identifying local uncertainties and errors from imagery requires new methods that improve current frequentist approaches (Datcu et al., 1998; Lasslop et al., 2010). The frequentist statistics use standard interpretation of probability where the event's probability is limited by its relative frequency and draws conclusions from likelihood estimates from the sample data (McCarthy, 2007). The Bayesian inference method expresses uncertainties in the model parameters in terms of probability. The parameter uncertainty quantification is achieved by using probability distributions for both priors and posteriors. The Bayesian inference method has been used in a number of discipline-specific applications such as remote sensing (Atkinson and Lewis, 2000), geographic information science (Crosetto and Tarantola, 2001; Grêt-Regamey and Straub, 2006) and ecology (Gorsevski, 2013; Iizumi et la., 2009; Patenaude et al., 2008; Wintle et al., 2003).

Thus, the aim of this project is to generate estimates of tree leaf area based on small-footprint LiDAR-derived measurements and to quantify the uncertainty associated with the parameter estimates in the prediction of LAI using Bayesian inference. The proposed approach intends to address the following three objectives: (1) to compare different ground-based measurements that are used for quantification of LAI estimates; (2) to develop predictive models that quantify spatial distribution of LAI from correlations between ground-based measurements and satellite derived indices; and (3) to account for uncertainty in parameter estimates associated with the prediction. The first objective intends to compare measurements from LAI-2200 Plant Canopy Analyzer and TLS C10 instruments which will be used to develop the spatial distribution model of LAI with satellite based vegetation indices. Finally, Bayesian inference using Markov Chain Monte Carlo (MCMC) simulation will be implemented to account for the uncertainty of parameter estimates through posteriors derived from prior probability from vegetation indices.

CHAPTER I. STUDY AREA

The study area is located in the Oak Openings Region in NW Ohio and extends into SE Michigan (Fig.1). The Oak Openings Preserve Metro Park is a rare ecosystem with an approximate area of 15 km^2 in the Lake Erie watershed and hosts a range of flora and fauna diversity. The region supports a mosaic of Great Lakes habitats including wet prairies, white oak savannas, Midwest sand barrens, black oak savanna with lupine barrens, and black oak and white oak woodland communities that are developed on a series of post-glacial beach ridges and swales. The major ecosystem in the region is the white and black oak savannas with both homogeneous and heterogeneous deciduous stands with a small mixture of conifers. A few developed areas are also present at the boundary of Metro Park.

The white and black savanna region is rich in white oaks (*Quercus alba*) and black oaks (*Quercus velutina)* whereas the Grassland ecosystems host species such as bluestem (*Schizachyrium scoparium*) and sandbur (*Cenchrus sp*) as well as various species of *Panicum*, big bluestem, (A*ndropogon gerardii*), and Indian grass (*Sorgastrum nutans)*. The sandy ecosystems are habitats for species such as Cafringed gentian (*Gentianopsis crinita*), goldenrods (*Solidago sps*.), blazing star (*Liatris spicata*), and cowbane (*Oxypolis rigidior*). In addition, this small park region provides important habitats to rare organisms including federal and state endangered species such as the Eastern Whip-poor-will (*Caprimulgus vociferous*) as well as the Karner Blue Butterfly (*Lycaeides melissa)* and persius Dusky Wing (*Erynnis persius)* that live on another rare plant species called Wild Blue Lupine (*Lupinus perennis*). These natural dispersions of ecosystems are controlled by several geological and climatological factors. Post-glacial beach sand belt deposited on bedrock of either Dolomite or Limestone with a general elevation range of 180 to 230 m act as the major geological basement of the region (Schetter, 2012). The region shows a humid continental climate with an annual temperature range of 10 $^{\circ}$C to 23 $^{\circ}$C and a mean annual precipitation of 81 cm. The average canopy height and the stand age are 24 m and 45 years respectively (ORNL, 2013; Schetter, 2012).

CHAPTER II. DATASETS AND METHODS

2.1. Terrestrial LiDAR data collection and pre-processing

The Terrestrial Laser Scanner (TLS), Leica ScanStation C 10, was used to acquire point cloud data during the summer of 2013 between June and August. The Leica C 10 scanner measures the traveling time of the emitted laser pulses and calculates the distances of the objects. The high-speed laser pulses are green waves of 532 nm with measurement accuracy of 2 – 6 mm. The scanner measurements are generated in a stepwise fashion by fast mirror rotations in horizontal and vertical directions. The field of view is 360 degrees in the horizontal direction and 270 degrees in the vertical direction. In addition, the Leica C 10 can capture images using a built-in camera that provide photorealistic 3-D model of the colored point clouds.

A total of 30 plots were scanned using a total of four scans for each plot to reduce the occlusion effect (Fig. 1). The summary scan layout for each location is shown in Fig. 2 (a). The position of four scans were set where S_1 is the plot center (home scan) and the other three scans S_2, S_3 and S_4 are the lateral scans placed at the border of the plot that is approximately at the circumference of 50 m radius from the center**.** In addition, four target poles were set as reference points (T_1, T_2, T_3 and T_4). The effective scanning range for detecting objects was limited to 100 m from the home scan. The auto adjusting, high-resolution integrated digital camera was set to capture the full range multi images simultaneously with point cloud data acquisition. To minimize the effect of double scans of each object, the data were collected during low wind conditions.

Co-registration was used to merge or fuse the home scan point cloud with the point clouds of the three lateral scans using Cyclone 8.0 software (Leica-Cyclone, 2013). The co-registration was supported by reference targets which were used to register and align the multiple scans with the reference coordinate frame. The permitted mean absolute error (MAE) associated with the co-registration was set to less than 0.026, which is automatically calculated by the software. The origin of the reference coordinate frame (X_0, Y_0, Z_0) was set at the center of the home scan, which represents the mapping coordinate system measured by Yuma Trimble. Fig. 3 displays a sample co-registered scan derived from a total of four individual scans. After removing the background noise the point clouds were segmented into smaller 3-D cylinders. The cylinder base of the original point cloud was centered at the home scan and was placed at 1 m height above the ground. This was done to avoid groundcover noise and for other consistency associated with the LAI-2200 data collection.

2.2. LAI-2200 plant canopy analyzer data collection

The LAI-2200 Plant Canopy Analyzer is a passive sensor, which is used to compute LAI among variety of other canopy structure attributes from radiation measurements. The instrument integrates a fish-eye optical sensor with five silicon detectors arranged in circular rings that sample radiation above and below canopy at five zenith angles simultaneously. The LAI-2200 measurements are acquired by leveling and viewing the sky, where detector 1 measures brightness directly overhead e.g., 7°, while detector 5 measures brightness of a ring centered at 68° zenith angle. The transmittance of below canopy reading is normalized by corresponding above canopy reading to calculate the LAI. The most accurate measurements are collected during the diffuse sky conditions but other alternatives for data collection include different device setting which use preselected view caps and masks or data collection that is carried out early mornings or late afternoons.

Within each site, a total of 9 observations per plot were collected by the LAI-2200 Plant Canopy Analyzer. Fig. 2 (b) shows the location of the LAI observations which are placed along eight principal compass directions (north, northeast, east, southeast, south, southwest, west, northwest) positioned and centered from the home scan. During the data collection process, to account and minimize effect of sunlit surfaces, heterogeneity of forest plots as well as the operator being in the field of view all the measurements used a 180° cap to mask the obstructions. At least one above canopy measurement that corresponds to each plot was acquired during the LAI- 2200 data collection. The below canopy collection included measurements from the areas of dense vegetation and sparse vegetation separately to minimize the edge effect. The two outermost ring readings (53° and 68°) were masked in the LAI calculation as open areas are not large enough to use those two rings to collect above canopy readings within the Metro Park.

2.3. Point cloud slicing

The initial point cloud from each 3-D cylinder consists of large number of points and creates difficulties with the processing of the data. Thus, to reduce the number of points in the cloud the data were segmented by slicing. The method applied here implemented circular point cloud segmentation using horizontal slicing direction. The sliced cross sections represent small cylinders with a base circle of 30 m radius and slices of 0.25 m thickness. Fig. 3 illustrates the horizontal slicing direction of the point cloud cylinder. The 0.25 m thickness of the sliced cylinders was selected arbitrarily but intended to minimize the point overlap associated with the conversion from 3-D real space into 2-D model space and to avoid a very thin slices with inadequate feature descriptions.

Additional hemispherical point cloud segmentation was implemented to two of the sample cloud data scans (same location) for the purpose of threshold identification using trees with foliage (leaf-on) and without foliage (leaf-off). Both cylinders with s base circle of 30 m radius were clipped into 2 m thick hemispheres. The 2 m segmentation thickness is an arbitrary value that was aimed to reduce beam return intensity variation. Fig. 4 show the hemispherical segmentation concept of the point cloud cylinder when foliage was present. The hemispherical segmentation was used to calibrate the intensity within each plot and to discern foliage from other non-photosynthetic material.

2.4. Separation of photosynthetically active from non-active components

The separation of non-photosynthetic components such as trunks and branches from other photosynthetically active material was accomplished on the basis of laser beam return intensities and estimates of proper separation thresholds. The intensity data is useful for data processing and visualization of the data ranges. For example, the solid targets (i.e., non-photosynthetic material) reflect strong incoming pulses which produce return pulses with sharp peaks. However, the return intensity is also a function of portion of beam hitting the target, surface homogeneity of the target, distance between the instrument and the target, angle of incidence and bidirectional reflectance distribution function (BRDF) of the target within the field of view (Beland et al., 2011).

To separate the non-photosynthetic from the photosynthetic components this approach required identification of multiple intensity threshold values. Thus, assuming that completely illuminated targets by the laser beam had Lambertian scattering properties, the intensities of the return signal became independent regardless of distances between the instrument and the target.

Also, since laser return intensity values recorded by the TLS were negative, an arbitrary value of 2000 was added to all measurements for the positive conversion and referred here as "modified intensities" (Eitel et. al., 2010). Fig. 5 (a) shows the relationship between modified intensity and distance. The figure shows that the intensity is directly influenced by the distance. At very close range (< 5 m) the intensity is low because the TSL requires a minimal operating distance but the general trend suggests that the TSL intensity decreases as the distance increases.

Fig. 5 (b) shows the probability density functions from beam intensity returns using the leaf-on and leaf-off point clouds. The hemispherical point cloud segmentation plot was used to generate the count of beam intensity returns. The 2 m thick hemispheres were proceeds by data binning technique for grouping and organizing the 3-D real space of the cloud. The vertical line in the plot is associated with the return intensity and represents the threshold value that separates foliage from wood. In the figure, the threshold value provides minimized misclassification of foliage and wood intensity returns. In the plot the LW are points of leaves misclassified as wood while WL represents points of wood that misclassified as leaves.

2.5. LAI estimates from orthographic and stereographic projection of point cloud data

The 3-D real space of each cylindrical segment was projected into 2-D model space (i.e., the X-Y plane) to generate orthographic projection view of the TLS data. The aim of this orthographic projection is to simplify the mathematical processing of the point cloud data and to help with the LAI estimates. Fig. 6 (a) shows a sample 2-D model space output of the orthographically projected TLS point cloud. Fig. 6 (b) shows an example of the final raster image that was generated from orthographically projected 2-D point clouds and used for the LAI estimates. The images were rasterized by point to raster algorithm using a cell size of 4 cm. The cell size was determined from the distance and point spacing relationship. The Fig.7 shows the graph of distances to the object against the spacing between two adjacent TLS points scanned from the object. The data set was developed by scanning a static article by changing its distance in 5 m increments to the TLS. The scanning was performed in controlled indoor environment to avoid the noise due to wind. The maximum point spacing of 0.04 m shown on the y-axis which is the coarsest resolution used for the analysis of orthographic images. Two sets of 2-D orthographic images, one from points before removing woods and the other after removing wooden sections (leaves only) were produced following this procedure.

To generate the hemispherical images from TLS point clouds, the stereographic projection was implemented. The hemispherical image production required Cartesian point cloud coordinates to be converted to spherical coordinates and subsequently projected into a surface of a sphere with 1 m radius (Zheng and Moskal 2012b). Fig. 8 (a) represents a unit sphere of the projected TLS points. The points in the unit sphere surface were stereographically projected to generate a 2-D model space. Fig. 8 (b) shows the 2-D raster image derived from the unit sphere. Two different sets of stereographic images were generated for representing foliage and wood material separately.

The LAI estimates for the projected raster images were calculated by the Gap Light Analyzer (GLA) 2.0 software (Frazer et al., 1999). The GLA freeware has been developed for processing hemispherical photos using daily diffuse, direct and total solar radiation transmittance that is compared for specified sky conditions and calendar dates for each hemispherical location. The GLA implements a linear averaging algorithm (Welles and Norman 1991) based on a

Poisson probability distribution and assumes that foliage is randomly distributed for the calculation of the LAI.

2.6. Vegetation Indices

Landsat TM images recorded on 06 June 2011 that coincide with an extensive ground data collection were acquired for the study area and used to generate spectral vegetation indices. Because the field measurements are time consuming, expensive, and inconvenient for large scale monitoring, spectral vegetation indices are often used to estimate LAI. Some of the advantages associated with the spectral vegetation indices are the simplistic derivation from satellite imagery and their robustness in reduction of spectral effects caused by external factors including atmosphere and soil backgrounds. In this study, for the prediction of LAI, multiple vegetation indices were computed and investigated. The two band (red and NIR) combinations of indices including both slope based and ratio based were computed and analyzed. The values of the cells from the vegetation indices were extracted by the coordinates of the plot centers. The point extraction used bilinear interpolation which is a distance-weighted average that used values from the four nearest pixels. The relationship between the LAI estimates and vegetation indices was analyzed by generalized linear models (GLM) for the selection of significant predictor variables which were used in a Bayesian framework. Table 1 shows the significant vegetation indices ($p < 0.05$) that were used for the development model of LAI estimates.

2.7. Bayesian linear regression framework

The Bayesian linear regression framework for parameter estimation consists of three key components including prior distribution, the likelihood function and the posterior distribution. The implementation of Bayesian linear regression (BLR) requires specification of the likelihood for the data, the form of the relationship between response and explanatory variables, and the prior distributions for regression coefficients or any unknown (nuisance) parameters. A simple Bayesian model is stated as:

$$y_i \;\cong\; N(\mu, \sigma^2), i = 1, \dots, n$$

$$\eta = \beta_0 + \sum_{j=1}^{k} \beta_p \, x_{ip}$$

$$\beta_p \;\cong\; priors \qquad (1)$$

where $y_1, y_2, \dots, y_n$ are the response variables for the random component that are assumed to be independent and normally distributed, the systematic component combines the covariates β_p's that form the linear predictor represented by $\eta = \beta_0 + \beta_1 x_1 + \beta_2 x_2 + \cdots + \beta_p x_p$, and finally the systematic and the random components are linked together via a link function $g(\mu) = \eta$. For GLMs the function *g* is taken to be the identity link so that we assume $\mu = \eta$. Using E to denote the expectation operator for calculating the mean the assumption is stated as:

$$\mu = E(y) = \beta_0 + \beta_1 x_1 + \beta_2 x_2 + \cdots + \beta_p x_p \qquad (2)$$

Finally, the Bayes' rule is used to compute the posterior distribution of the continuous β_p parameters where beliefs about the parameter are represented as probability density functions or pdfs. The Bayes' rule states that the posterior pdfs of the parameters is proportional to the product of the likelihood function and the prior pdfs as:

$$p(\beta, \sigma^2 | y, X) \;\propto\; p(y | X, \beta, \sigma^2) p(\beta | \sigma^2) p(\sigma^2) \qquad (3)$$

where $p(\beta|\sigma^2)p(\sigma^2)$ is the prior distribution and the $p(y|X,\beta,\sigma^2)$ is the likelihood given that the posterior distribution of $p(\beta,\sigma^2|y,X)$. Thus, the posterior distribution of each parameter is determined through Bayes' rule and defines the overall belief and uncertainties associated with the parameters.

In this study, the LAIs measured by the Plant Canopy Analyzer and derived from the TLS data represent the dependent variables while the significant vegetation indices that were scaled between 0 and 255 represent the independent covariates in the development of the predictive models. The predictive models were developed by implementation of BLR framework which calculated uncertainties for the significant covariates from posterior parameter distributions with 95% credible intervals. The Open source Bayesian Inference Using Gibbs sampling version 3.2.2 (OpenBUGS) software (MRC Biostatistic Unit, Cambridge, UK; http://www.mrc-bsu.cam.ac.uk/software/bugs/) (Lunn et al., 2000) was used to calculate the uncertainties in parameter estimates. The software runs the Bayesian model with MCMC simulation to generate the results of the posterior parameter estimates using random samples which are conditioned on previous estimates in each implemented chain. In this study, multiple simultaneous chains were tested to resample the posterior distribution and to understand convergence. The convergence was depicted from overlapped and intertwined chain patterns from history and trace plots. After the determination of the convergence, different iteration trails were tested to produce posterior estimates. The reported simulations for the estimated regression coefficients here are based on at least 50,000 iterations. The simulations also used different burn-in thresholds for finding acceptable starting points and thinning rates to increase parameter mixing and reduce high posterior correlations between parameters. Finally, Moran's *I* test was used to test the spatial autocorrelation from the residuals for all the models.

CHAPTER III. RESULTS

3.1. Comparison of LAI estimates

Fig. 9 shows the comparison of the six different LAIs that were measured by the Plant Canopy Analyzer and calculated from the TLS measurements. The LAI-2200 and the Le represent the measurements derived from the hand-held Plant Canopy Analyzer while the rest of the LAIs were derived from TLS measurements. The estimates derived from the Plant Canopy Analyzer used caps with narrower view (e.g., 45˚ field of view) to depict the canopy that is most likely to be foliage. Thus in the case of the LAI-2200 the resulted values represent the canopy which is automatically corrected for clumping. The effective LAI values (Le) were derived by adjusting the LAI-2200 estimates by apparent clumping factor at each location. On the other hand, the TLSO are the LAI estimates derived by orthographic projection while the TLSS are the LAI estimates derived by stereographic projection. Unlike TLSO and TLSS which estimate only the foliage, the TLSO_W and TLSS_W estimate both foliage and wooden biomass.

In Fig. 9, the scatterplot results are based on samples from all 30 plots and show strong overall correlations between the six different LAI estimates. The bivariate Pearson correlation coefficients (r) range between 0.51 and 0.99 which are shown above the diagonal. The highest observed correlation is between the estimates from the Plant Canopy Analyzer (LAI-2200 and Le) while the lowest correlation is between the estimates from TLSO_W and TLSS_W. However estimates that separate photosynthetically active from non-active components derived by orthographic projection show stronger correlation (r = 0.88) than estimates derived by stereographic projection (r = 0.82). In addition, the scatterplot results show that the hand-held Plant Canopy Analyzer has slightly stronger correlation with the TLS orthographic projection estimates which include foliage and wooden biomass (r = 0.60). The TLS stereographic projection that considers only foliage correlates better with the hand-held Plant Canopy Analyzer (r = 0.61). However, reasonable correlations are present between the different TLS estimates.

In the figure, the values of the LAI estimates shown on the plot axis are also different. The low values are most likely to represent the sparse vegetation and canopy gaps while the high values are most likely to represent the dense vegetation. The lowest values are associated with the orthographic projection that considers only foliage (0.5 - 2.0) while the highest values are associated with stereographic projection (3.5 – 8.5) that includes foliage and wooden biomass. The range of values from the hand-held Plant Canopy Analyzer is the most similar to the stereographic projection that includes only foliage.

In this study, it is apparent that the hand-held Plant Canopy Analyzer and the TLS instrument yielded different LAI ranges and estimates. To evaluate the absolute accuracy of each method for LAI estimates and the superiority of the methods is difficult because it requires a reference measurement such as destructive sampling. In the study area there is no previous estimates or reference measurements from destructive sampling to generate absolute LAI. As such, it is difficult to draw a firm conclusion regarding the relative accuracy of the different techniques that were used to generate LAI estimates or the advantages associated with the of the new laser scanning methodology. However, on the positive side the relatively strong relationships between different methods holds several advantages that can be used to correct expensive and labor intensive measurements from TLS by less expensive and portable LAI-2200 instrument. Additionally, the use of less expensive instrument simplifies the data collection and processing that can be corrected to resemble TLS data collection that is adjusted for foliage or wooden biomass. Another aspect that needs to be explored is the applicability of the estimates. For instance additional field measurements can be used for understanding the fluctuations of LAI ranges with different land cover or vegetation structure.

3.2. Development of LAI models

The results from the BLR are shown in Table 2. The table shows the predictive models, the significant covariates, the coefficients and their posterior distributions for the six LAIs. As shown, the number of significant covariates ($p < 0.05$) in the predictive LAI models differs. Interestingly, almost all the models derived from LAI measurements that separate foliage from the rest of the biomass are more complex than the models derived from LAI measurements that consider both foliage and wooden biomass. For instance, the models derived from the hand-held Plant Canopy Analyzer (i.e., LAI-2200 and Le) use only one significant covariate which is WDVI. The purpose of the WDVI covariate is to enhance vegetation signals by minimizing soil background effects through red and NIR bands. The models derived from the TLS measurements that include both foliage and wooden biomass use only one significant covariate (WDVI) in the case of the orthographic projection (TLSO_W) and two significant covariates (DVI and SAVI) in the case of the stereographic projection (TLSS_W). Finally, the two predictions associated with LAI that involve only foliage (Models 4 and 6) are the most complex and have identical sets of significant covariates including NDVI, SAVI, and PVI3. All those indices in Models 4 and 6 are commonly used to correct the influence of soil brightness at areas with low vegetation cover. In addition, the covariates used in the models consist of at least one vegetation index (i.e., NDVI) which depicts the abundance of green biomass as a function of red to NIR transmittance ratio.

The residuals from the predictive models are shown in Fig.10 where the predicted LAIs are plotted on the *x*-axis while the residuals are plotted on the *y*-axis. As shown in the plots the models that involve both foliage and wooden biomass predict values with higher residual ranges. For instance, the LAI estimates that consider foliage and wooden biomass have considerably more scatter than the estimates that consider only foliage. The predicted values associated with the orthographic projection (TLSO) that consider only foliage, have the least error among the six different models. The largest modeling error appears to be with the measurement generated by the hand-held Plant Canopy Analyzer.

Furthermore, the assessment of the model's residuals for spatial autocorrelation used Moran's *I* statistics shown in Fig.11. The sloped regression lines are plotted for all graphs using standardized predictions. The graphs are divided into four quadrants: high-high (upper right) and low-low (lower left) for positive spatial autocorrelation; and high-low (lower right) and low-high (upper left) for negative spatial autocorrelation. The positive spatial autocorrelation signifies occurrences of neighboring areas which are similar while the negative spatial autocorrelation signifies occurrences of neighboring areas which are dissimilar. The trends of the sloped regression lines suggest that the top three plots are most likely to be associated with positive autocorrelation while the lower three with negative autocorrelation . However, the inference for the Moran's *I* test which used permutation procedure against the null hypothesis indicated no presence of spatial autocorrelation for all models based on $p > 0.05$ values.

Fig.12 illustrates the spatial predictions of the LAIs developed by the six models from Table 2. The LAI estimates in the plots have been scaled between 0 and 6 for visualization and comparison of spatial patterns generated from the models. The top three plots of Fig. 12 (a), (b), and (c) which were derived from the WDVI correlations show similar predictive patterns. For instance, in those plots the abundance of low LAI (< 2) values across the study area is strongly emphasized especially in open areas, sparse canopy, and coniferous stands. Although high LAI (> 4) predictions are also present, the high LAI areas are constrained by smaller geographical areas that have homogeneous deciduous forest with dense canopies. The intermediate LAI values are most likely associated with sparse deciduous forests. The low LAI predictions associated with DVI and the SAVI covariates shown in Fig. 12 (e) depict large contiguous areas which are water bodies, forest openings and savannas. However, this model does not differentiate between the dense and the sparse vegetation. Finally, the plots in Fig. 12 (d) and (f) which predict foliage, derived from NDVI, SAVI, and PVI3 show different predictive patterns from the rest of the plots. The plots do not emphasize the strong discern between vegetation structure especially the difference between open areas and dense forest stands.

3.3. Uncertainty of parameter estimates

The results in Table 2 present the posterior inferences of mean, standard deviation, median and 95% credible intervals of all the parameters considered within 2.5% and 97.5% range. The positive coefficients of parameter estimates describe that the LAI will increase as the values of the predictor variable increases. The negative coefficients display the inverse relationship of the predictors with the LAIs. Based on the standard deviation and the range of coefficients within 95% credible intervals illustrated in the Table 2, all the models which use a single predictor variable show a very low variation or the uncertainty. The highest uncertainty or the deviance around mean was observed in the parameters for Model 6 which is the stereographic projection that includes only foliage. From the three models which are associated with WDVI, the lowest uncertainty resulted in the Model 3 (SD = 0.002) which is the orthographic projection with foliage and wooden biomass. The highest uncertainty resulted from the hand-held Plant Canopy Analyzer derived data which is corrected for apparent clumping effect (*SD* = 0.004). The NDVI uncertainties were relatively lower for the orthographic projection than for the stereographic projection. The SAVI and the PVI3 uncertainties had similar pattern as NDVI.

Fig. 13 (a) and (b) illustrates the mean LAI prediction and its standard deviation from the six models. The values associated with the mean LAI in Fig. 13 (a) vary between 0 and 7 and the histogram that accompanies the figure shows the distribution of the mean LAI values. The histogram show that the LAI estimates are slightly skewed to the left and most of the estimates range between 3 and 5. The predicted LAI estimates appear to be consistent with the generated expectations based on the very few forest openings and relatively well forested area.

The standard deviation map in Fig. 13 (b) shows the spatial uncertainties from the predictions. The histogram in the figure shows the standard deviation in terms of departure from the mean estimate. The most pronounced uncertainties (reddish and orange regions) of LAI estimates appear to have been generated by under predicted values but the map shows uncertainties generated from over predicted estimates especially in open areas. However, the highest uncertainty was observed in the areas with very low vegetation density associated with conifers and mixed forests (the yellowish regions).

CHAPTER IV. DISCUSSION

The results from this study revealed that field measured LAI from the hand-held Plant Canopy Analyzer and TLS instrument are highly correlated. TLS based LAI estimates can clearly overcome limitations of the hand-held method and separate foliage from wooden material but also the high correlations suggest that there is a chance for obtaining the same results from the hand-held method in conjunction with empirical modeling. However, there are many differences between the two approaches that would require additional future work. For instance the TLS is invariant to light incident angle but other conditions such as wind or foliage heterogeneity may influence the estimates. Also the work reported here is based on implemented random data sampling approach but accounting and stratifying for different vegetation types, structure and forest associations perhaps would improve the understanding of the relationships between the LAI estimates.

The significance of several Landsat TM derived vegetation indices including WDVI, DVI, NDVI, SAVI, and PVI3 was used for the BLR model development (Boegh et al., 2002, Eklundh et al., 2003, Gong et al., 1995). Although these indices detect the vegetation based on the same red and NIR signals, they are differentially impacted by the canopy homogeneity, structure, gaps and bare soil as well as topography. For example, the NDVI detects the green vegetation and does not consider the soil noise. Also, the NDVI is mostly independent from topography and it is insensitive at areas with more than 80% vegetation cover (Qi et al., 1994). The WDVI, SAVI, DVI and PVI3 use different implications not only to detect the vegetation but also to correct the influence of soil brightness. The SAVI is sensitive for a high range of vegetation densities as well as soil noise levels where the WDVI has limitations at areas with fewer gaps (Qi et al., 1994).

The modeling results obtained from the combination of indices NDVI, PVI3 and SAVI that predict only foliage maybe the most comprehensive as the NDVI captures the green intensity, the PVI3 corrects the vegetation signal for soil brightness and the SAVI is sensitive for a long range of soil and vegetation conditions. Such results are implicative of capturing LAI based on density and gap distribution. This is also supported by observing forest patterns and heterogeneity from imagery but some of the main limitations with those indices is the differentiation between vegetation types such as conifers and deciduous and forest structure. This differs from the predictions that do not distinguish between foliage and wooden biomass where only WDVI is used in the predictions. The models generated by the WDVI do not capture adequately the presence in the canopy gaps. Also, the modeled residuals suggested that the spared of residuals is the highest with the WDVI especially from measured LAI by the hand-held Plant Canopy Analyzer. On the other hand the foliage models were associated with the lowest error and spared of residuals. Therefore, one of the benefits from the TLS-based estimates is to quantify LAI associated with foliage using satellite-based products.

Furthermore, the uncertainties with parameter estimate were different but with the increase of model complexity the uncertainties in the parameters also increased. At this point it is not clear which of the vegetation factors (i.e., including distribution, heterogeneity, structure, and type of vegetation) influenced the uncertainties of the LAI estimates the most. However, the advantage of this methodology is the ability to identify and quantify the uncertainties while considering the factors that influence LAI estimates. A detailed future study with different sampling strategies that involve the structure and heterogeneity is required to explain the influence of these factors and LAI predictions separately.

CHAPTER V. CONCLUSION

Field measurements from LAI 2200 Plant Canopy Analyzer and terrestrial laser scans from Leica ScanStation C10 were used in this study in order to measure and predict LAI in the Oak Openings region in NW Ohio. The TLS collected point cloud data from a total of 30 plots by using four scans per plot. The co-registered and processed cloud data was used to separate the photosynthetically active from non-active components and to produce stereographic and orthographic projection models for quantifying LAI. The measured and the predicted LAI were used for comparisons of LAIs, model development, and for quantifying uncertainties associated with the predictions.

A total of six different LAIs were compared to examine differences and relationships between the estimates. The results suggest strong overall correlations between the six different LAI estimates but since there is no reference measurements it is difficult to evaluate the absolute accuracy of the individual methods. In addition a total of six different BLR models were developed using the relationships between LAIs and vegetation indices that were derived from Landsat imagery. The advantage of the Bayesian approach is that the iterative calculation result in probability distributions of the posterior estimates of the parameters which are used for through assessment of uncertainties. The BLR models suggested that the model complexity increases for LAI predictions of foliage compared to the prediction of both foliage and wooden biomass. For instance, the LAI models associated with the foliage used NDVI, SAVI, and PVI3 covariates while the LAI model associated with the foliage used only WDVI for the hand-held Plant Canopy Analyzer and SAVI and DVI for the TSL estimates.

The results of the modeled LAIs showed that uncertainty analysis in parameter estimates can be further evaluated for understanding model fit and LAIs generated by different methods. Although, accurate prediction of LAI estimates is difficult because of the complex vegetation patterns and the structure, modeled showed that uncertainty analysis in parameter estimates can be used to understand the influence of each predictor in the LAI estimate. However, future consideration for this research would require the need for data collection based on vegetation homogeneity and structure, validation of TLS based measurements as well as LAI 2200 hand-held Plant Canopy Analyzer data with most accurate LAI measurements such as destructive sampling, dependency of LAI measurements with projection, and selection and testing of additional vegetation indices or satellite products.

REFERENCES

Asner, G. P., Scurlock, J. M., & A Hicke, J. (2003). Global synthesis of leaf area index observations: implications for ecological and remote sensing studies. *Global Ecology and Biogeography*, *12*(3), 191-205.

Atkinson, P. M., & Lewis, P. (2000). Geostatistical classification for remote sensing: an introduction. *Computers & Geosciences*, *26*(4), 361-371

Baret, F., & Guyot, G. (1991). Potentials and limits of vegetation indices for LAI and APAR assessment. *Remote sensing of environment*, *35*(2), 161-173.

Béland, M., Widlowski, J. L., Fournier, R. A., Côté, J. F., & Verstraete, M. M. (2011). Estimating leaf area distribution in savanna trees from terrestrial LiDAR measurements. *Agricultural and Forest Meteorology*, *151*(9), 1252-1266.

Boegh, E., Søgaard, H., Broge, N., Hasager, C. B., Jensen, N. O., Schelde, K., & Thomsen, A. (2002). Airborne multispectral data for quantifying leaf area index, nitrogen concentration, and photosynthetic efficiency in agriculture.*Remote Sensing of Environment*, *81*(2), 179-193.

Bréda, N. J. (2003). Ground-based measurements of leaf area index: A review of methods, instruments and current controversies. *Journal of Experimental Botany, 54*(392), 2403-2417.

Bulcock, H., & Jewitt, G. (2010). Spatial mapping of leaf area index using hyperspectral remote sensing for hydrological applications with a particular focus on canopy interception. *Hydrol.Earth Syst.Sci, 14*, 383-392.

Cao, M., & Woodward, F. I. (2002). Net primary and ecosystem production and carbon stocks of terrestrial ecosystems and their responses to climate change.*Global Change Biology*, *4*(2), 185-198.

Chasmer, L., Hopkinson, C., & Treitz, P. (2006). Investigating laser pulse penetration through a conifer canopy by integrating airborne and terrestrial lidar. *Canadian Journal of Remote Sensing*, *32*(2), 116-125.

Chason, J. W., Baldocchi, D. D., & Huston, M. A. (1991). A comparison of direct and indirect methods for estimating forest canopy leaf area. *Agricultural and Forest Meteorology*, *57*(1), 107-128.

Chen, J. M., Black, T. A., & Adams, R. S. (1991). Evaluation of hemispherical photography for determining plant area index and geometry of a forest stand. *Agricultural and Forest Meteorology*, *56*(1), 129-143.

Chen, J. M., & Cihlar, J. (1995). Plant canopy gap-size analysis theory for improving optical measurements of leaf-area index. *Applied optics*, *34*(27), 6211-6222.

Chen, J. M., Rich, P. M., Gower, S. T., Norman, J. M., & Plummer, S. (1997). Leaf area index of boreal forests: Theory, techniques, and measurements.*Journal of Geophysical Research: Atmospheres (1984–2012)*, *102*(D24), 29429-29443.

Chen, J. M., Pavlic, G., Brown, L., Cihlar, J., Leblanc, S. G., White, H. P., Pellikka, P. K. E. (2002). Derivation and validation of canada-wide coarse-resolution leaf area index maps using high-resolution satellite imagery and ground measurements. *Remote Sensing of Environment, 80*(1), 165-184.

Clevers, J. G. P. W. (1988). The derivation of a simplified reflectance model for the estimation of leaf area index. *Remote Sensing of Environment*, *25*(1), 53-69.

Côté, J., Widlowski, J., Fournier, R. A., & Verstraete, M. M. (2009). The structural and radiative consistency of three-dimensional tree reconstructions from terrestrial lidar. *Remote Sensing of Environment, 113*(5), 1067-1081.

Crosetto, M., & Tarantola, S. (2001). Uncertainty and sensitivity analysis: tools for GIS-based model implementation. *International Journal of Geographical Information Science*, *15*(5), 415-437.

Datcu, M., Seidel, K., & Walessa, M. (1998). Spatial information retrieval from remote-sensing images. I. Information theoretical perspective. *Geoscience and Remote Sensing, IEEE Transactions on*, *36*(5), 1431-1445.

Davidson, D. P. (2002). Sensitivity of ecosystem net primary productivity models to remotely sensed leaf area index in a montane forest environment (Doctoral dissertation, Lethbridge, Alta.: University of Lethbridge, Faculty of Arts and Science).

Dewey, J. C., Roberts, S. D., & Hartley, I. (2006). A comparison of tools for remotely estimating leaf area index in loblolly pine plantations. *Proceedings of the 13th Biennial Southern Silvicultural Research Conference Gen. Tech. Rep. SRS*, *92*, 71-75.

Dong, J., Kaufmann, R. K., Myneni, R. B., Tucker, C. J., Kauppi, P. E., Liski, J., Hughes, M. K. (2003). Remote sensing estimates of boreal and temperate forest woody biomass: Carbon pools, sources, and sinks. *Remote Sensing of Environment, 84*(3), 393-410.

Dufrêne, E., & Bréda, N. (1995). Estimation of deciduous forest leaf area index using direct and indirect methods. *Oecologia*, *104*(2), 156-162.

Eitel, J. U., Vierling, L. A., & Long, D. S. (2010). Simultaneous measurements of plant structure and chlorophyll content in broadleaf saplings with a terrestrial laser scanner. *Remote sensing of environment*, *114*(10), 2229-2237.

Eklundh, L., Hall, K., Eriksson, H., Ardö, J., & Pilesjö, P. (2003). Investigating the use of Landsat thematic mapper data for estimation of forest leaf area index in southern Sweden. *Canadian Journal of Remote Sensing*, *29*(3), 349-362.

Fassnacht, K. S., Gower, S. T., Norman, J. M., & McMurtric, R. E. (1994). A comparison of optical and direct methods for estimating foliage surface area index in forests. *Agricultural and Forest Meteorology, 71*(1), 183-207.

Foody, G. M., & Atkinson, P. M. (Eds.). (2002). *Uncertainty in Remote Sensing and GIS.* Chichester:John Wiley & Sons.

Frazer, G. W., Canham, C. D., & Lertzman, K. P. (1999). Gap Light Analyzer (GLA), Version 2.0: Imaging software to extract canopy structure and gap light transmission indices from true-colour fisheye photographs, user's manual and program documentation. *Simon Fraser University, Burnaby, British Columbia, and the Institute of Ecosystem Studies, Millbrook, New York*, *36*.

Gamon, J. A., Field, C. B., Goulden, M. L., Griffin, K. L., Hartley, A. E., Joel, G., & Valentini, R. (1995). Relationships between NDVI, canopy structure, and photosynthesis in three Californian vegetation types. *Ecological Applications*, 28-41.

Gilabert, M. A., González-Piqueras, J., Garcıa-Haro, F. J., & Meliá, J. (2002). A generalized soil-adjusted vegetation index. *Remote Sensing of Environment*, *82*(2), 303-310.

Gong, P., Pu, R., & Miller, J. R. (1995). Compact Airborne Spectrographic lmager Data. *Photogrammetric Engineering & Remote Sensing*, *61*(9), 1107-1117.

Gorsevski, P. V. (2013). Using Bayesian inference to account for uncertainty in parameter estimates in modelled invasive flowering rush. *Remote Sensing Letters*, *4*(3), 279-287.

Groeneveld, D. P. (1997). Vertical point quadrat sampling and an extinction factor to calculate leaf area index. *Journal of arid environments*, *36*(3), 475-485.

Grêt-Regamey, A., & Straub, D. (2006). Spatially explicit avalanche risk assessment linking Bayesian networks to a GIS. *Natural Hazards and Earth System Science*, *6*(6), 911-926.

Haboudane, D., Miller, J. R., Tremblay, N., Zarco-Tejada, P. J., & Dextraze, L. (2002). Integrated narrow-band vegetation indices for prediction of crop chlorophyll content for application to precision agriculture. *Remote Sensing of Environment, 81*(2–3), 416-426.

Haboudane, D., Miller, J. R., Pattey, E., Zarco-Tejada, P. J., & Strachan, I. B. (2004). Hyperspectral vegetation indices and novel algorithms for predicting green LAI of crop canopies: Modeling and validation in the context of precision agriculture. *Remote Sensing of Eenvironment*, *90*(3), 337-352.

Hashimoto, H., Wang, W., Milesi, C., White, M. A., Ganguly, S., Gamo, M., & Nemani, R. R. (2012). Exploring simple algorithms for estimating gross primary production in forested areas from satellite data. *Remote Sensing*,*4*(1), 303-326.

Henning, J. G., & Radtke, P. J. (2006). Ground-based laser imaging for assessing three dimensional forest canopy structure. *Photogrammetric Engineering and Remote Sensing, 72*(12), 1349.

Hosoi, F., & Omasa, K. (2006). Voxel-based 3-D modeling of individual trees for estimating leaf area density using high-resolution portable scanning lidar.*Geoscience and Remote Sensing, IEEE Transactions on*, *44*(12), 3610-3618.

Hosoi, F., & Omasa, K. (2007). Factors contributing to accuracy in the estimation of the woody canopy leaf area density profile using 3D portable Lidar imaging. *Journal of Experimental Botany*, *58*(12), 3463-3473.

Houghton, R. (2005). Aboveground forest biomass and the global carbon balance. *Global Change Biology, 11*(6), 945-958.

Huang, P., & Pretzsch, H. (2010). Using terrestrial laser scanner for estimating leaf areas of individual trees in a conifer forest. *Trees-Structure and Function*, *24*(4), 609-619.

Huete, A. R. (1988). A soil-adjusted vegetation index (SAVI). *Remote Sensing of Environment, 25*(3), 295-309.

Iizumi, T., Yokozawa, M., & Nishimori, M. (2009). Parameter estimation and uncertainty analysis of a large-scale crop model for paddy rice: application of a Bayesian approach. *Agricultural and forest meteorology*, *149*(2), 333-348.

Jonckheere, I., Fleck, S., Nackaerts, K., Muys, B., Coppin, P., Weiss, M., & Baret, F. (2004). Review of methods for in situ leaf area index determination: Part I. Theories, sensors and hemispherical photography. *Agricultural and Forest Meteorology*, *121*(1), 19-35.

Jupp, D. L., Culvenor, D. S., Lovell, J. L., Newnham, G. J., Strahler, A. H., & Woodcock, C. E. (2009). Estimating forest LAI profiles and structural parameters using a ground-based laser called 'Echidna®. *Tree Physiology*, *29*(2), 171-181.

Kandwal, R., Jeganathan, C., Tolpekin, V., & Kushwaha, S. P. S. (2009). Discriminating the invasive species,'Lantana'using vegetation indices. *Journal of the Indian Society of Remote Sensing*, *37*(2), 275-290.

Kwak, D. A., Lee, W. K., & Cho, H. K. (2007). Estimation of LAI using LiDAR remote sensing in forest. In *ISPRS Workshop on Laser Scanning and SilviLaser*.

Lasslop, G., Reichstein, M., Papale, D., Richardson, A. D., Arneth, A., Barr, A. & Wohlfahrt, G. (2010). Separation of net ecosystem exchange into assimilation and respiration using a light response curve approach: critical issues and global evaluation. *Global Change Biology*, *16*(1), 187-208

Lee, K., Cohen, W. B., Kennedy, R. E., Maiersperger, T. K., & Gower, S. T. (2004). Hyperspectral versus multispectral data for estimating leaf area index in four different biomes. *Remote Sensing of Environment, 91*(3), 508-520.

Lim, K., Treitz, P., Wulder, M., St-Onge, B., & Flood, M. (2003). LiDAR remote sensing of forest structure. *Progress in Physical Geography, 27*(1), 88-106.

Liu, J., Chen, J. M., Cihlar, J., & Chen, W. (1999). Net primary productivity distribution in the BOREAS region from a process model using satellite and surface data. *Journal of Geophysical Research*, *104*(D22), 27735-27754.

Leica Cyclone 3D point cloud processing software. (2013). Retrieved 06/10, 2013, http://www.leica-geosystems.us/en/Leica-Cyclone_6515.htm.

Lovell, J. L., Jupp, D. L. B., Newnham, G. J., & Culvenor, D. S. (2011). Measuring tree stem diameters using intensity profiles from ground-based scanning lidar from a fixed viewpoint. *ISPRS Journal of Photogrammetry and Remote Sensing, 66*(1), 46-55.

Lunn, D.J., Thomas, A., Best, N., and Spiegelhalter, D. (2000) WinBUGS -- a Bayesian modelling framework: concepts, structure, and extensibility. *Statistics and Computing*, **10**:325--337.

Mencuccini, M., & Grace, J. (1995). Climate influences the leaf area/sapwood area ratio in scots pine. *Tree Physiology, 15*(1), 1-10.

McCarthy, M. A. (2007). *Bayesian methods for ecology*. Cambridge: Cambridge University Press.

Moskal, L. M., & Zheng, G. (2011). Retrieving forest inventory variables with terrestrial laser scanning (TLS) in urban heterogeneous forest. *Remote Sensing, 4*(1), 1-20.

Neumann, H. H., Den Hartog, G., & Shaw, R. H. (1989). Leaf area measurements based on hemispheric photographs and leaf-litter collection in a deciduous forest during autumn leaf-fall. *Agricultural and Forest Meteorology*,*45*(3), 325-345.

Patenaude, G., Hill, R. A., Milne, R., Gaveau, D. L., Briggs, B. B. J., & Dawson, T. P. (2004). Quantifying forest above ground carbon content using LiDAR remote sensing. *Remote Sensing of Environment*, *93*(3), 368-380.

Patenaude, G., Milne, R., Van Oijen, M., Rowland, C. S., & Hill, R. A. (2008). Integrating remote sensing datasets into ecological modelling: a Bayesian approach. *International Journal of Remote Sensing*, *29*(5), 1295-1315

Potter, C., Klooster, S., Crabtree, R., Huang, S., Gross, P., & Genovese, V. (2011). Carbon fluxes in ecosystems of Yellowstone National Park predicted from remote sensing data and simulation modeling. *Carbon Balance and Management*, *6*(1), 1-16.

Qi, J., Chehbouni, A., Huete, A. R., Kerr, Y. H., & Sorooshian, S. (1994). A modified soil adjusted vegetation index. *Remote sensing of environment*, *48*(2), 119-126.

Rouse, J. W., Haas, R. H., &hell, J. A., Deering, D. W., & Harlan, J. C. (1974), Monitoring the vernal advancement of retrogradation of natural vegetation, NASA / GSFC, Type III, Final Report, Greenbelt, MD, p. 371.

Reich, P. B., Turner, D. P., & Bolstad, P. (1999). An approach to spatially distributed modeling of net primary production (NPP) at the landscape scale and its application in validation of EOS NPP products. *Remote Sensing of Environment*, *70*(1), 69-81.

Richardson, A. D., Dail, D. B., & Hollinger, D. Y. (2011). Leaf area index uncertainty estimates for model–data fusion applications. *Agricultural and Forest Meteorology*, *151*(9), 1287-1292.

Richardson, A. J., & Weigand, C. L. (1977). Distinguishing vegetation from soil background information. *Photogrammetric Engineering and Remote Sensing*,*43*(12).

Running, S. W., Nemani, R. R., Heinsch, F. A., Zhao, M., Reeves, M., & Hashimoto, H. (2004). A continuous satellite-derived measure of global terrestrial primary production. *Bioscience*, *54*(6), 547-560.

Schetter, T. A. (2012). *A multiscale spatial analysis of Oak Openings plant diversity with implications for conservation and management*. Bowling Green State University.

Turner, D. P., Ollinger, S. V., & Kimball, J. S. (2004). Integrating remote sensing and ecosystem process models for landscape-to regional-scale analysis of the carbon cycle. *BioScience*, *54*(6), 573-584.

Turner, D. P., Cohen, W. B., Kennedy, R. E., Fassnacht, K. S., & Briggs, J. M. (1999). Relationships between leaf area index and landsat TM spectral vegetation indices across three temperate zone sites. *Remote Sensing of Environment, 70*(1), 52-68.

U.S. Department of Agriculture - Forest Service (USDA-FS), 2013. Forests and Carbon Storage. Retrieved February 11, 2013, http://www.fs.fed.us/ccrc/topics/forests-carbon/.

United Nations Framework Convention on Climate Change (UNFCCC). (n.d.). Retrieved February 19, 2013, http://unfccc.int/2860.php.

Van der Zande, D., Hoet, W., Jonckheere, I., van Aardt, J., & Coppin, P. (2006). Influence of measurement set-up of ground-based LiDAR for derivation of tree structure. *Agricultural and Forest Meteorology*, *141*(2), 147-160.

Van Gardingen, P., Jackson, G., Hernandez-Daumas, S., Russell, G., & Sharp, L. (1999). Leaf area index estimates obtained for clumped canopies using hemispherical photography. *Agricultural and Forest Meteorology, 94*(3), 243-257.

Welles, J., & Norman, J. (1991). Instrument for indirect measurement of canopy architecture. *Agronomy Journal, 83*(5), 818-825.

Wintle, B. A., McCarthy, M. A., Volinsky, C. T., & Kavanagh, R. P. (2003). The use of Bayesian model averaging to better represent uncertainty in ecological models. *Conservation Biology*, *17*(6), 1579-1590.

WU, J., & LI, H. (2006). Uncertainty analysis in ecological studies: an Overview, *Scaling and Uncertainty Analysis in Ecology*, 45-66.

Yao, T., Yang, X., Zhao, F., Wang, Z., Zhang, Q., Jupp, D., Strahler, A. (2011). Measuring forest structure and biomass in new england forest stands using echidna ground-based lidar. *Remote Sensing of Environment, 115*(11), 2965-2974.

Zaehle, S., Sitch, S., Prentice, I. C., Liski, J., Cramer, W., Erhard, M., & Smith, B. (2006). The importance of age-related decline in forest NPP for modeling regional carbon balances. *Ecological Applications*, *16*(4), 1555-1574.

Zhao, M., Heinsch, F. A., Nemani, R. R., & Running, S. W. (2005). Improvements of the MODIS terrestrial gross and net primary production global data set. *Remote Sensing of Environment, 95*(2), 164-176.

Zhao, F., Yang, X., Schull, M. A., Román-Colón, M. O., Yao, T., Wang, Z., & Strahler, A. H. (2011). Measuring effective leaf area index, foliage profile, and stand height in New England forest stands using a full-waveform ground-based lidar. *Remote Sensing of Environment*, *115*(11), 2954-2964.

Zheng G., Moskal L.M, 2009. Retrieving Leaf Area Index (LAI) Using Remote Sensing: Theories, Methods and Sensors. *Sensors*, 9(4), 2719-2745.

Zheng, G., & Moskal, L. M. (2012a). Computational-geometry-based retrieval of effective leaf area index using terrestrial laser scanning. *Institute of Electrical and Electronic Engineers*, 50(10), 3958-3969.

Zheng, G., & Moskal, L. M. (2012b). Spatial variability of terrestrial laser scanning based leaf area index. *International Journal of Applied Earth Observation and Geoinformation, 19*, 226-237.

APPENDIX A. FIGURES

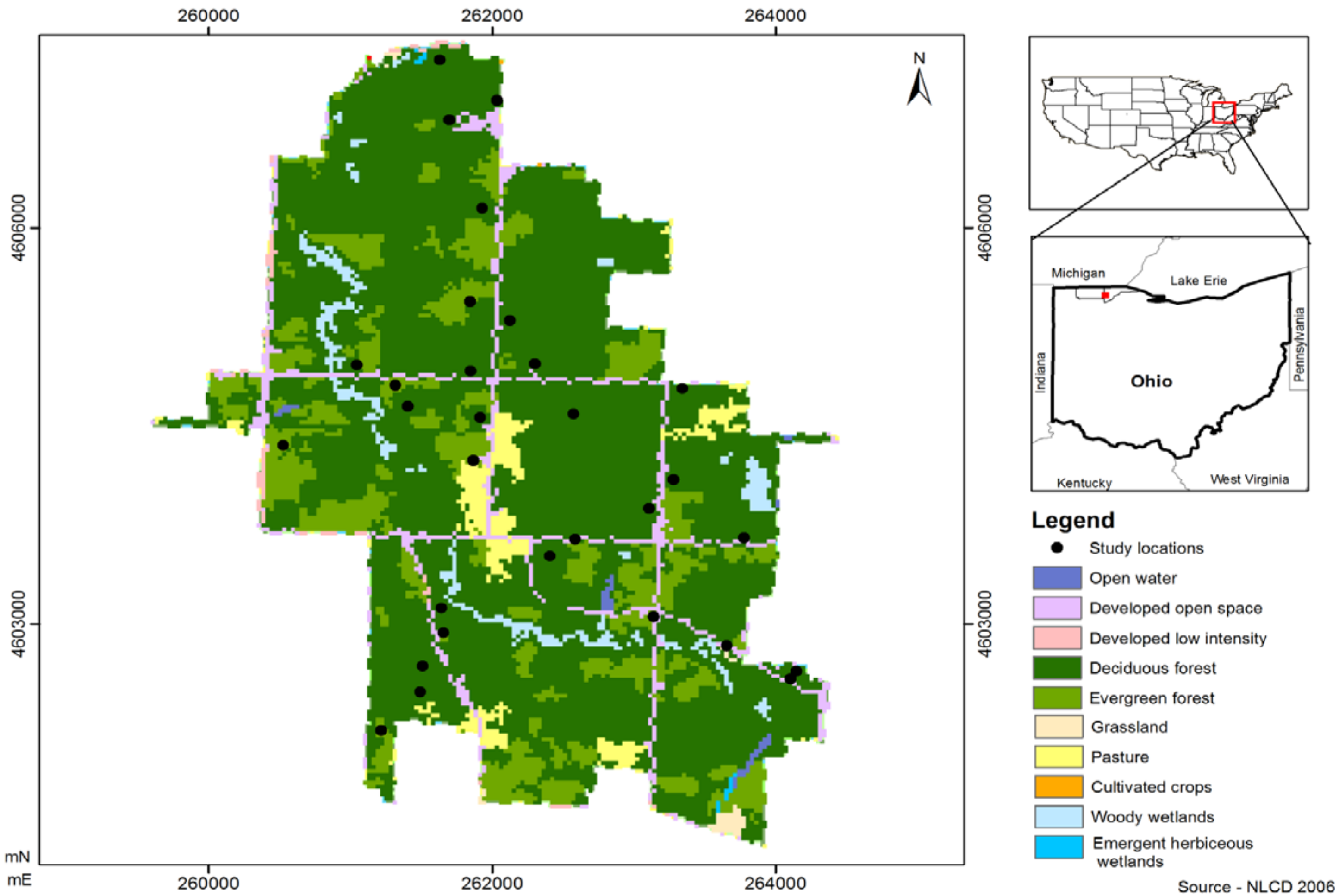

Fig. 1: Location map of study plots at Oak opening Metro Park, Toledo

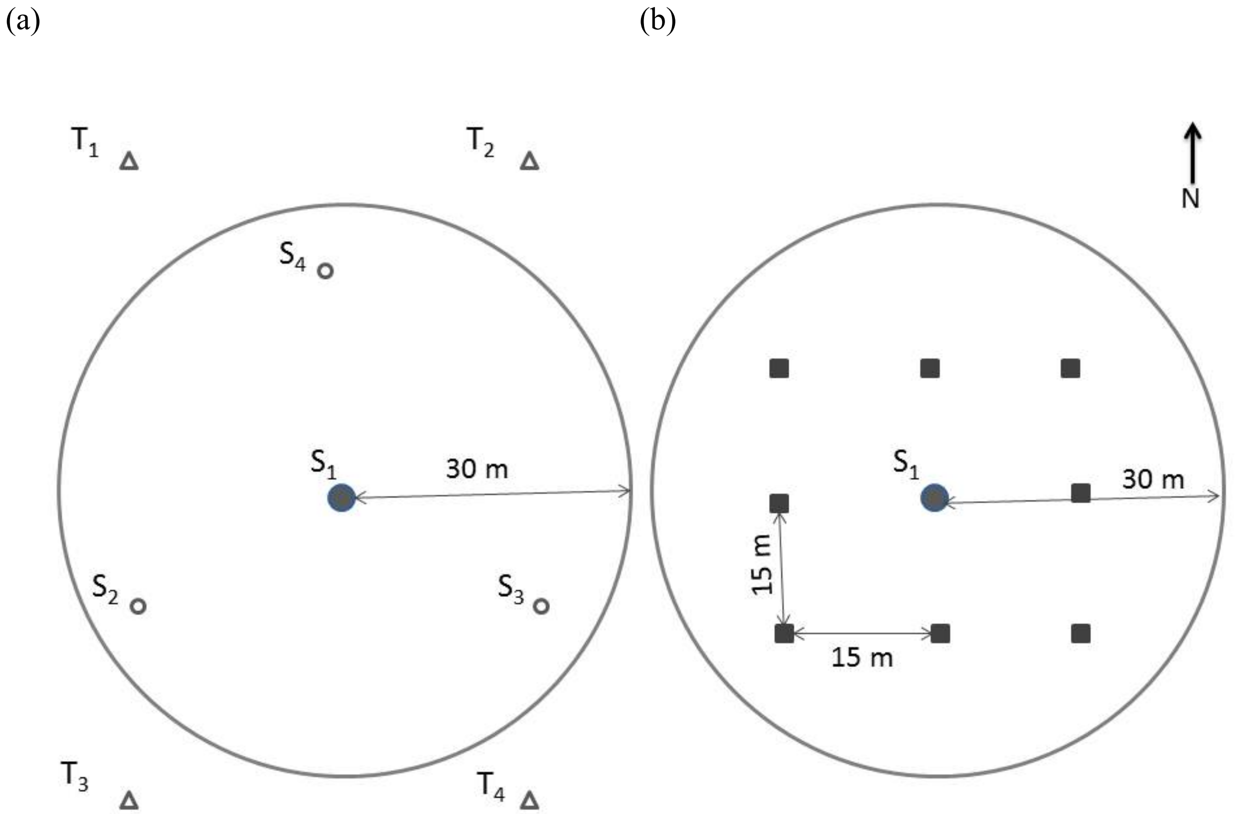

Fig. 2: Schematic diagram of filed data collection for (*a*) Leica ScanStation C10; and (*b*) the LAI-2200 Plant Canopy Analyzer for each study plot

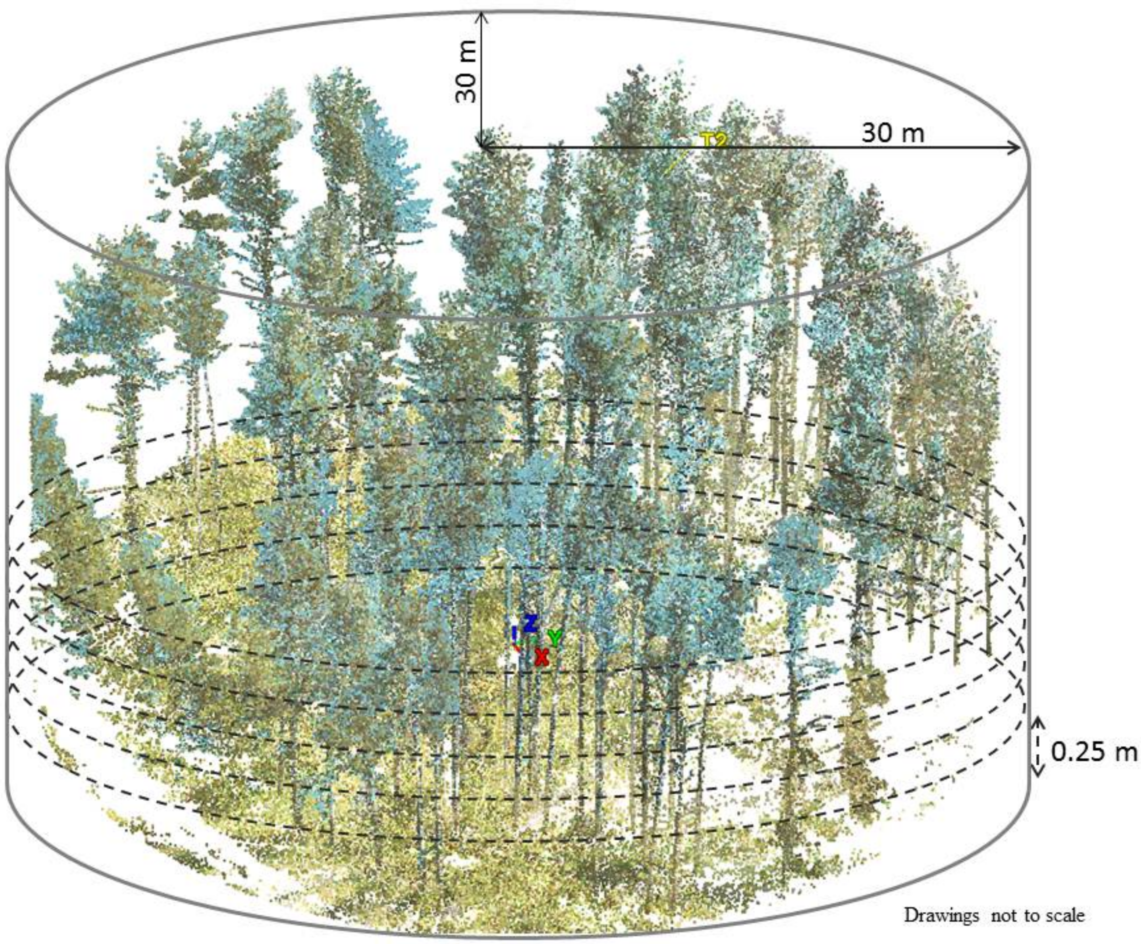

Fig. 3: Co-registered 30 m radius point cloud cylinder clipped into 0.25 m thick horizontal slices

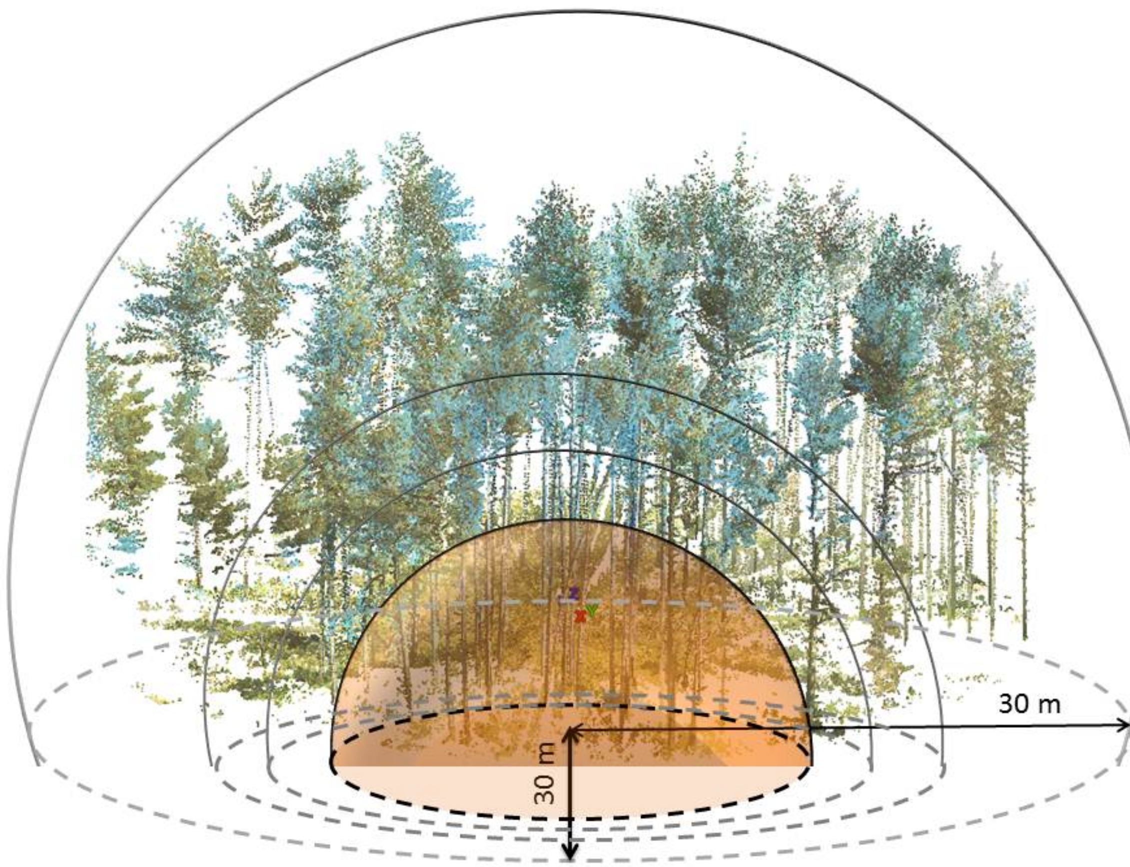

Fig. 4: Co-registered 30 m radius point cloud cylinder clipped into 2 m thick spherical slices

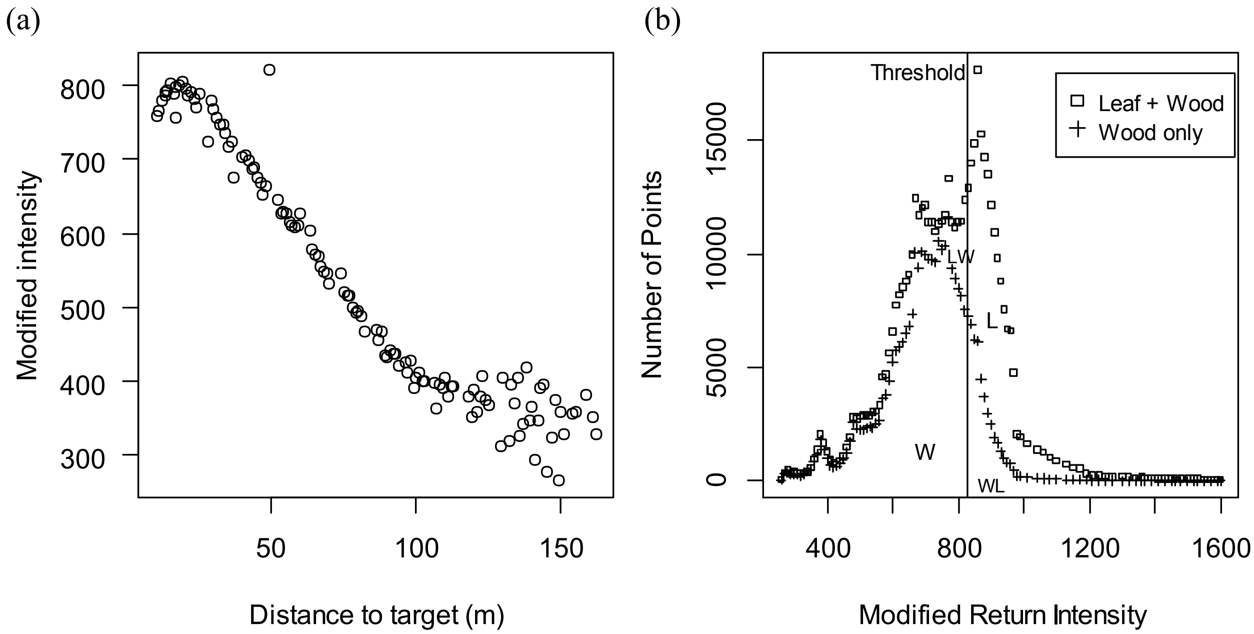

Fig 5: TLS point intensity and distance relationships (a) distance – object modified return intensity relationship (b) sample leaf - wood histogram using modified intensity and distance range between 16 – 18 m from the TLS(L- leaves only, W- Wood only, WL – Wood misclassified as leaves and LW – leaves misclassified as wood)

(a) (b)

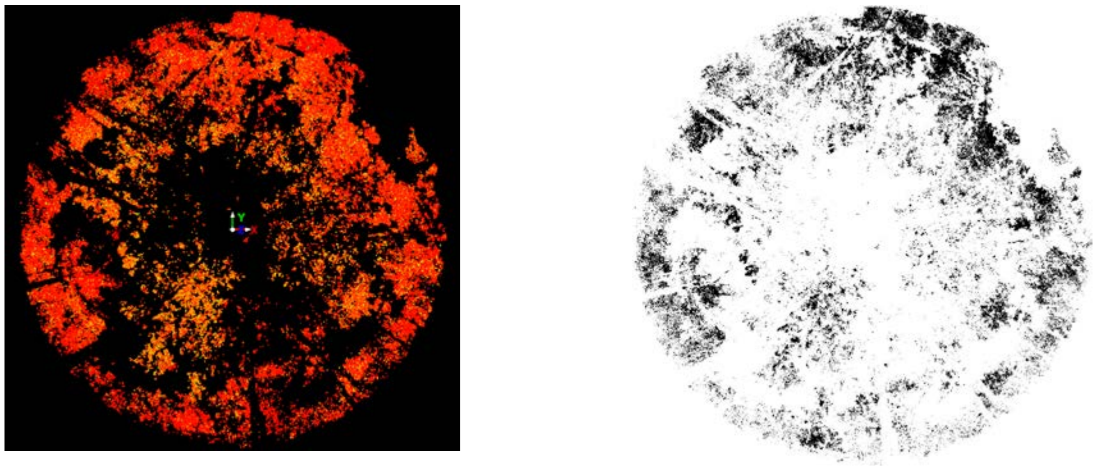

Fig. 6: Projection of sample point cloud showing (a) the orthographic view from TLS; and (b) rasterized image from the orthographic view

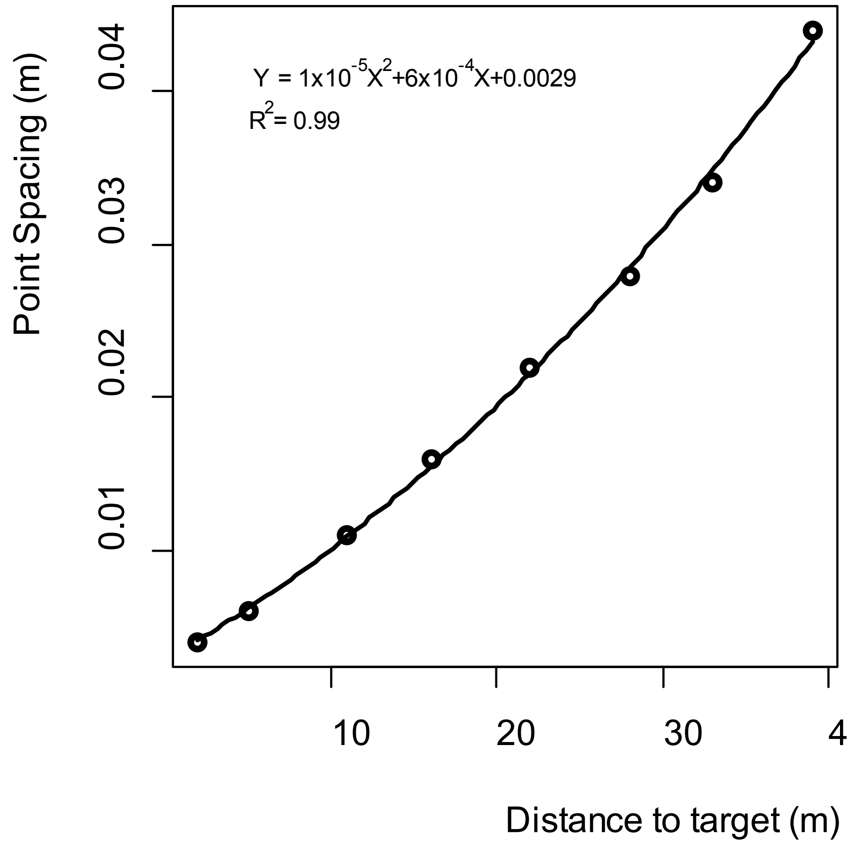

Fig 7: Point spacing variation with distance to the TLS C 10

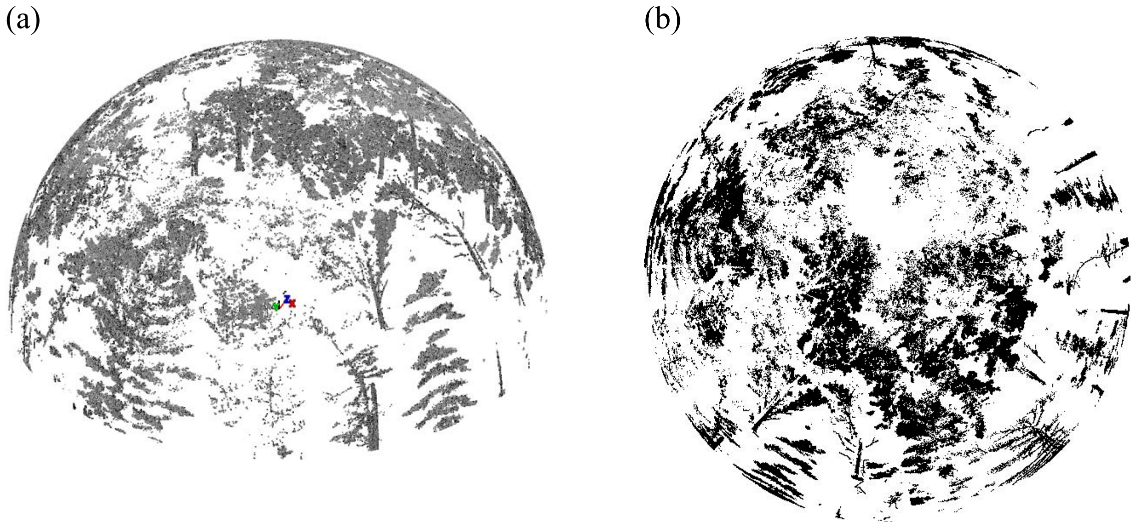

Fig 8: Hemispherical images derived from TLS point clouds where (a) are points in a unit sphere surface; and (b) is stereographically projected rasterized image

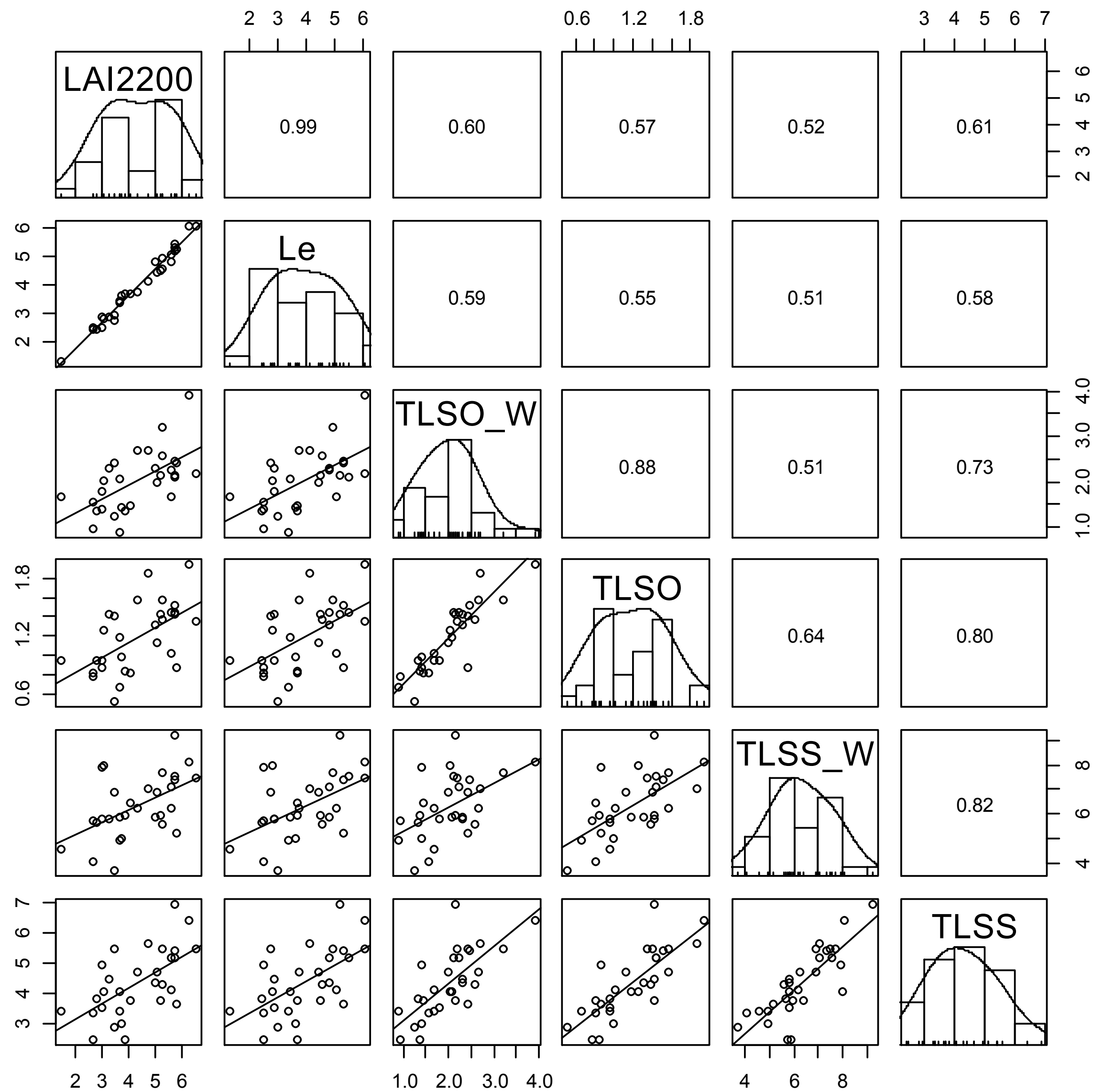

Fig. 9: Comparison between LAIs measured from LAI 2200 Plant Canopy Analyzer and TLS measurements (LAI2200- LAI from LAI 2200 Plant Canopy Analyzer, Le - Effective LAI from Plant Canopy Analyzer, TLSO_W – Orthographic LAI with both wood and foliage biomass, TLSO orthographic LAI with only foliage, TLSS_W – Stereographic LAI with both wood and foliage biomass and TLSS – stereographic LAI with only foliage)

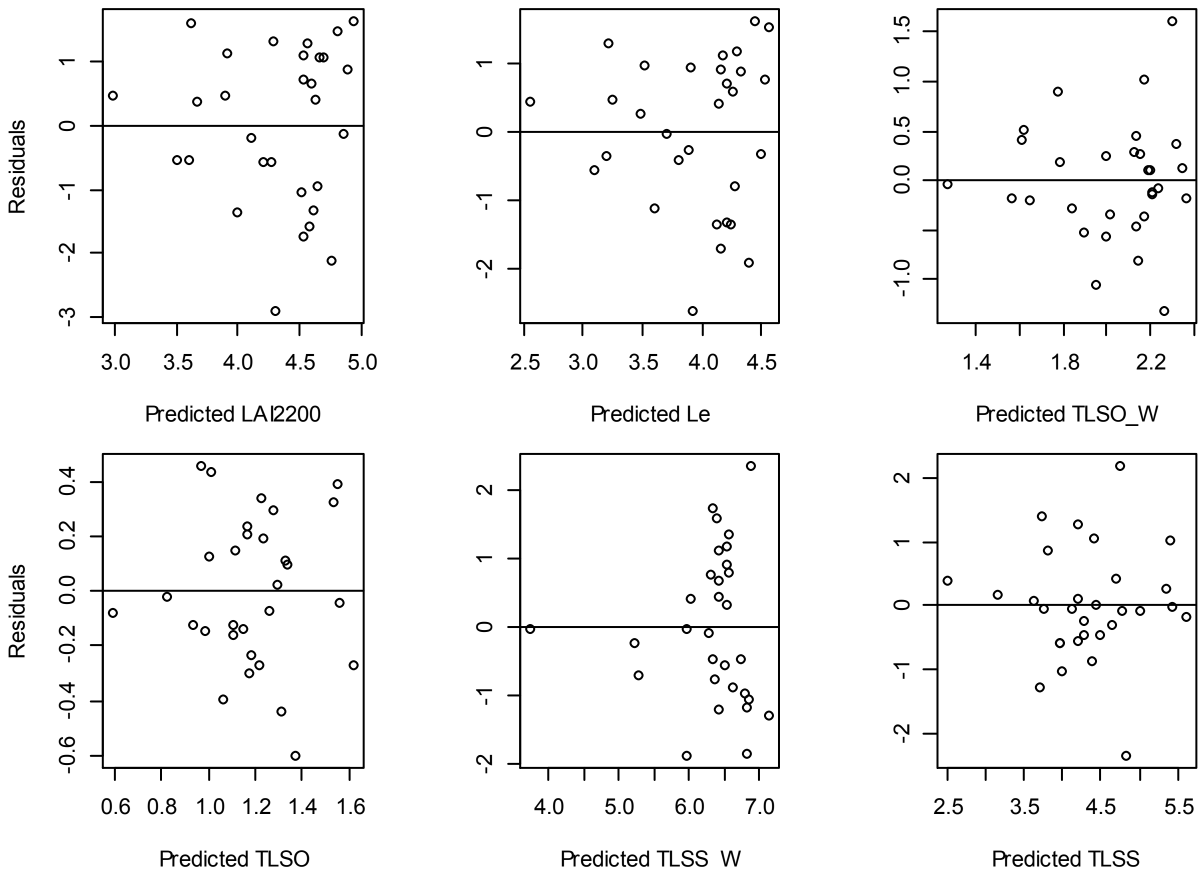

Fig. 10: Residual plots for the six different types of LAI measurements

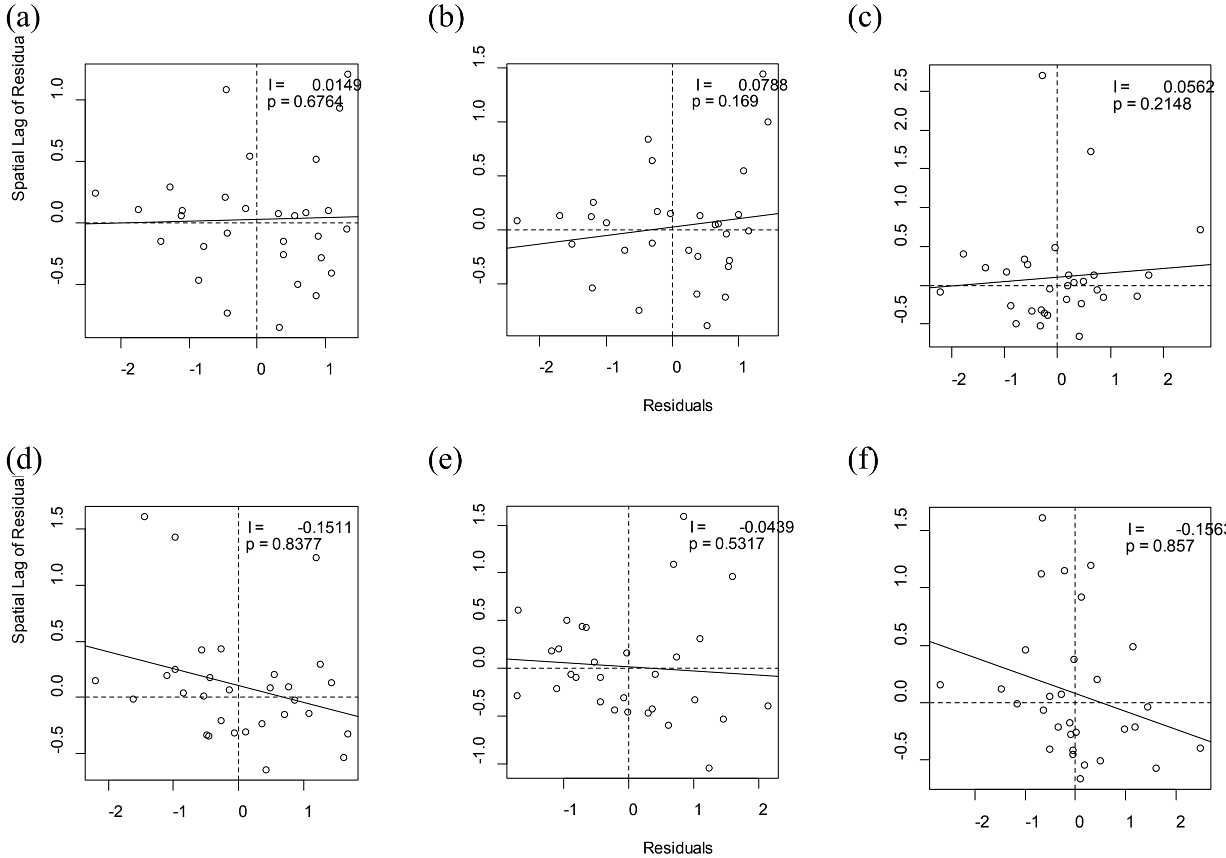

Fig.11 : Plots of Moran's I test for assessing spatial autocorrelation of model residuals (a) for LAI 2200 data (Morans's $I = 0.0149$) (b) for Le data (Morans's $I = 0.0788$) (c) for TLSO_W data (Morans's $I = 0.0562$) (d) for TLSO data (Morans's $I = -0.1511$) (e) for TLSS_W data (Morans's $I = -0.0439$); and (f) for TLSS data (Morans's $I = -0.1563$)

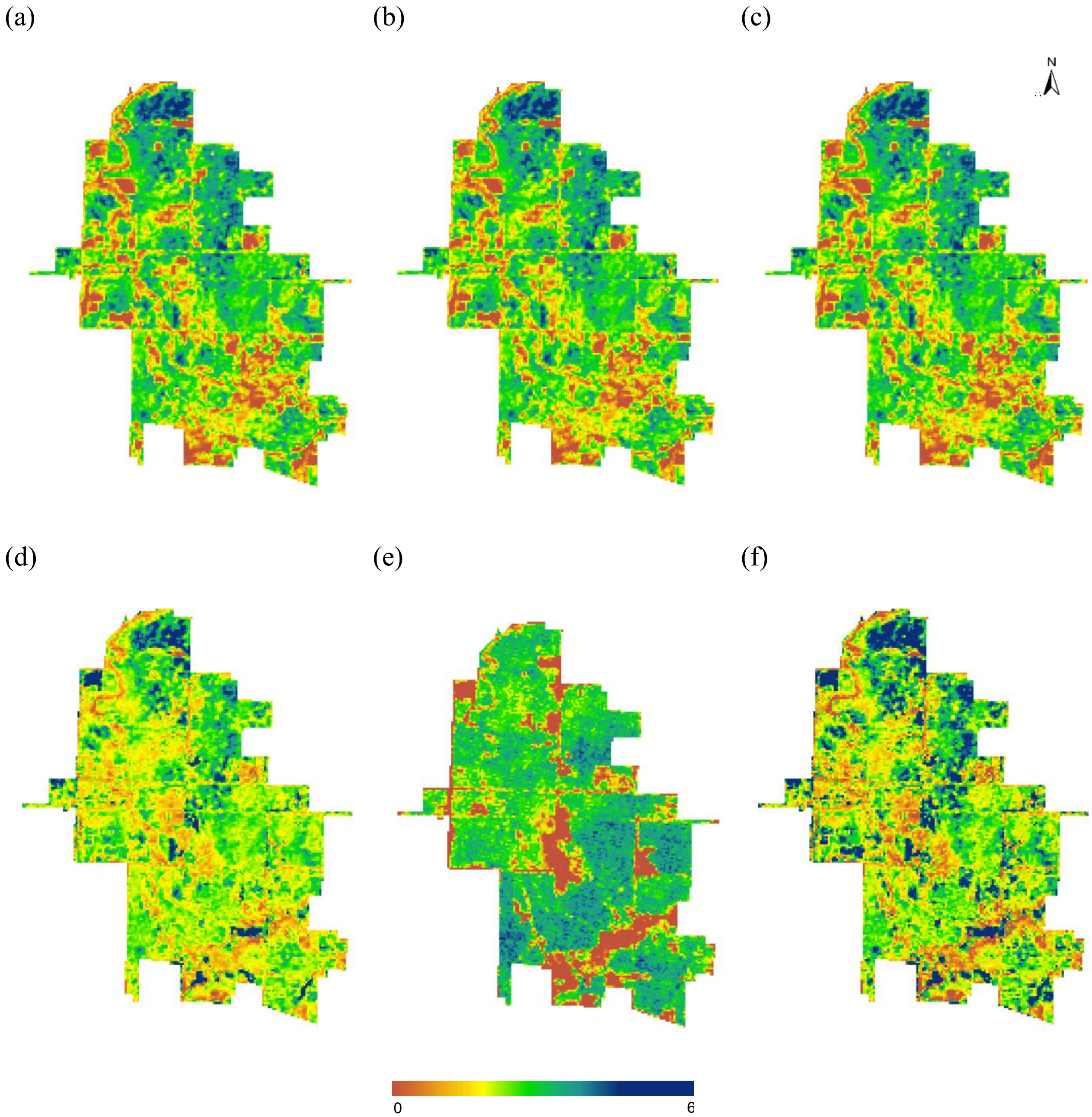

Fig. 12: Estimated LAIs using BLR mean values for (a) LAI 2200, (b) Le, (c) TLSO_W, (d) TLSO, (e) TLSS_W; and (f) TLSS data

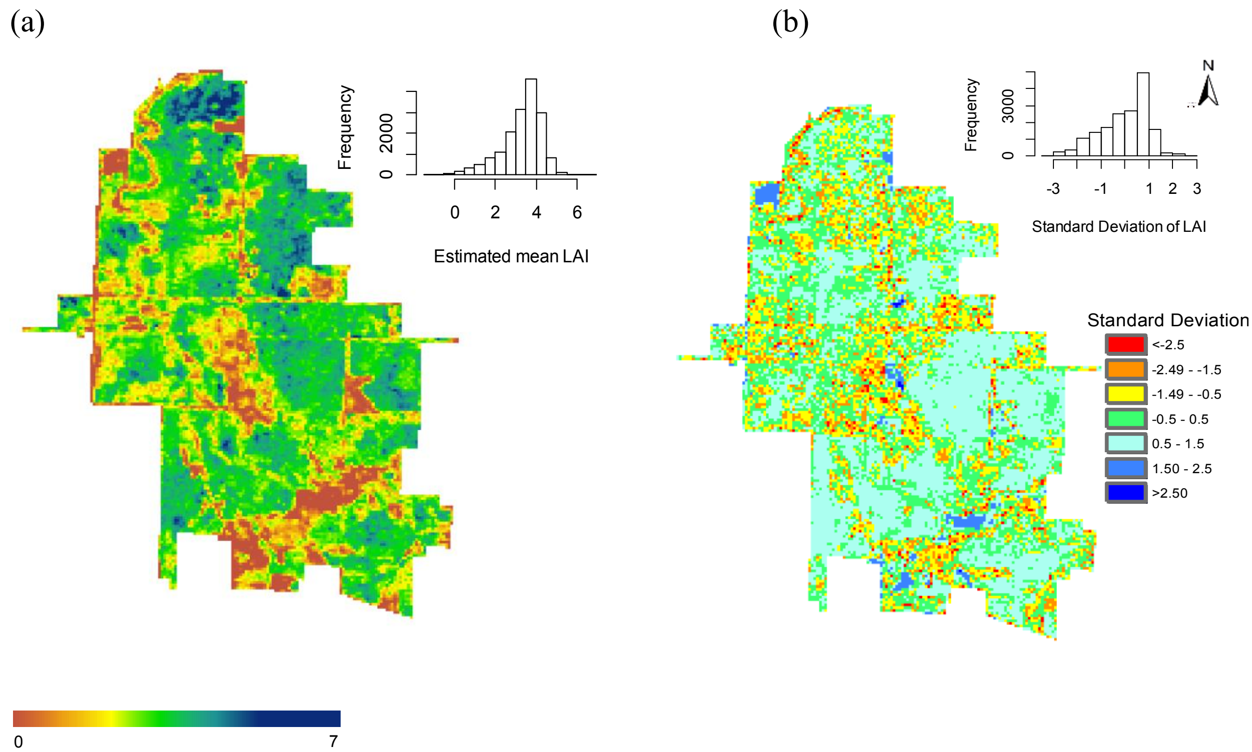

Fig.13: (a) Mean LAI estimates and (b) standard deviation of LAI estimates using the six predictive models

APPENDIX B: TABLES

Table 1. Significant vegetation indices used for model development

Vegetation Index	Derivation based on	Equation	Reference
Normalized Difference Vegetation Index (NDVI)	Slope based	$\text{NDVI} = \frac{(\text{NIR}-\text{Red})}{(\text{NIR}+\text{Red})}$	Rouse et al.,1974
Soil Adjusted Vegetation Index (SAVI)	Slope based (soil noise)	$\text{SAVI} = \frac{(\text{NIR}-\text{Red})}{(\text{NIR}+\text{Red})} + (1 + \text{L})$	Huete (1988)
Difference Vegetation Index (DVI)	Distance based	$\text{DVI} = \text{m} * \text{NIR} - \text{Red}$	Richardson and Wiegand, 1977)
Weighted Difference Vegetation Index (WDVI)	Distance based (soil noise)	$\text{WDVI} = \text{NIR} - \text{m} * \text{Red}$	Clevers, 1989
Perpendicular Vegetation Index III (PVI3)	Distance based	$\text{PVI3} = (\text{c} * \text{NIR}) - (\text{m} * \text{Red})$	Qi et al., 1994
NIR – Red reflectance, Red – Red Reflectance, L- Soil Adjustment factor (used as 0.5), m- Slope of the soil line, c – intercept of the soil line			

Table 2: Uncertainty estimates of model coefficients using Bayesian inference with MCMC simulation

Parameters	Mean	SD	2.5%	25%	Median	75%	97.5%
Model 1:	**LAI-2200 = 3.020 + 0.007 * WDVI**						
Intercept	3.020	0.701	1.60	2.574	3.036	3.486	4.360
WDVI	0.007	0.004	0.00	0.005	0.007	0.010	0.015
Model 2:	**Le = 2.582 + 0.008 * WDVI**						
Intercept	2.582	0.639	1.288	2.176	2.597	3.007	3.803
WDVI	0.008	0.003	0.001	0.005	0.008	0.010	0.015
Model 3:	**TLSO_W = 1.288 + 0.004 * WDVI**						
Intercept	1.288	0.342	0.595	1.070	1.295	1.515	1.941
WDVI	0.004	0.002	0.001	0.003	0.004	0.005	0.008
Model 4:	**TLSO = 0.596 + 0.394 * NDVI – 0.511 * SAVI + 0.133 * PVI3**						
Intercept	0.596	0.248	0.108	0.434	0.597	0.760	1.086
NDVI	0.394	0.144	0.107	0.301	0.393	0.493	0.678
SAVI	-0.511	0.188	-0.881	-0.640	-0.509	-0.390	-0.138
PVI3	0.133	0.048	0.037	0.102	0.133	0.166	0.229
Model 5:	**TLSS_W = 3.752 + 0.006 * DVI + 0.008 * SAVI**						
Intercept	3.752	0.907	1.980	3.158	3.757	4.357	5.521
DVI	0.006	0.004	-0.001	0.004	0.006	0.009	0.013
SAVI	0.008	0.004	0.000	0.006	0.008	0.011	0.016
Model 6:	**TLSS = 2.493 + 1.349 * NDVI - 1.747 * SAVI + 0.452 * PVI3**						
Intercept	2.493	0.790	0.934	1.973	2.494	3.013	4.055
NDVI	1.349	0.460	0.434	1.051	1.344	1.664	2.256
SAVI	-1.747	0.599	-2.928	-2.157	-1.741	-1.360	-0.556
PVI3	0.452	0.154	0.145	0.352	0.450	0.558	0.756

APPENDIX C: CODES

1. Code for separating TLS point cloud based on distance and intensity (In R statistical software)

```
#set environment
setwd("F:/RSoft/new pro/input")

#remove objects
rm(list=objects())

#take start time
ts1 <- Sys.time()

intThreshold <- 850

#read all input files
inputDir <- paste(getwd(),"/",sep="")
resultDir <- paste(getwd(),"/../result/",sep="")
files <- list.files(pattern=".pts")

#Looping through files in the directory
for(f in 1:length(files))
{
 inFilePath <- paste(inputDir, files[f], sep="")
 baseFileName <- gsub(".pts", "", files[f])
 resultFilePath <- paste(resultDir, "sep_", baseFileName, ".txt", sep="")

 if(baseFileName =='8'){
  intThreshold <- 825
 } else if(baseFileName =='10'){
     intThreshold <- 825
 } else if(baseFileName =='12'){
  intThreshold <- 925
 } else if(baseFileName =='14'){
  intThreshold <- 875
 } else if(baseFileName =='16'){
  intThreshold <- 850
 } else if(baseFileName =='18'){
  intThreshold <- 800
 } else if(baseFileName =='20'){
  intThreshold <- 800
 } else if(baseFileName =='22'){
  intThreshold <- 850
 } else if(baseFileName =='24'){
```

```
  intThreshold <- 850
} else if(baseFileName =='26'){
  intThreshold <- 825
} else if(baseFileName =='28'){
  intThreshold <- 825
} else if(baseFileName =='30'){
  intThreshold <- 825
} else if(baseFileName =='32'){
  intThreshold <- 800
} else if(baseFileName =='34'){
  intThreshold <- 800
} else if(baseFileName =='36'){
  intThreshold <- 800
} else if(baseFileName =='38'){
  intThreshold <- 800
} else if(baseFileName =='40'){
  intThreshold <- 800
} else if(baseFileName =='42'){
  intThreshold <- 800
} else if(baseFileName =='44'){
  intThreshold <- 800
} else {
  intThreshold <- 850
}

print(paste("Processing file",files[f],"started..."))
print(resultFilePath)

mydata <- read.table(inFilePath,header = T, sep ='')
attach(mydata)

num <- 0
num <- dim(mydata)
num[1]

#filteredData <- subset(mydata, Int > 850)
filteredData <- subset(mydata, intensity > (intThreshold - 2000))

write.table(filteredData, resultFilePath, sep="\t", row.names=F)

detach(mydata)
rm(mydata)
rm(filteredData)
print(paste("Processing file",files[f],"ended..."))
}
```

```
ts2 <- Sys.time()
print(ts2 - ts1)
```

2. Code behind the conversion of Cartesian coordinates to stereographic projection (In R statistical software)

```
#set environment

setwd("E:/Oak/37/sphere_data/sep_37")

#remove objects
rm(list=objects())

#take start time
ts1 <- Sys.time()

 calcDist <- function(p){
  p[5] <- sqrt((p[1])^2 + (p[2])^2 + (p[3])^2)

  p[1] <- (p[1])/(p[5])
  p[2] <- (p[2])/(p[5])
  p[3] <- (p[3])/(p[5])

  return(p)
 }

 calcSt <- function(q){
  zenith <- acos(q[3])/(q[8])
  st_zenith <- ((pi/2)*tan(zenith/2))

  q[1] <- (q[8])*sin(st_zenith)*cos(q[7])
  q[2] <- (q[8])*sin(st_zenith)*sin(q[7])
  q[3] <- (q[8])*cos(st_zenith)

  return(q)
 }

#read all input files
inputDir <- paste(getwd(),"/",sep="")
resultDir <- paste(getwd(),"/../unit/",sep="")

files <- list.files(pattern=".txt")
```

```
#Looping through files in the directory
for(f in 1:length(files))
{
  ts2 <- Sys.time()

  inFilePath <- paste(inputDir, files[f], sep="")
  resultFilePath <- paste(resultDir, "unit_", files[f], sep="")

  print(inFilePath)
  print(resultFilePath)

  mydata <- read.table(inFilePath,header=T,sep='\t')

  mydata <- apply(mydata, 1, calcDist)
  mydata <- t(mydata [1:4,])

  write.table(mydata, resultFilePath, row.names = F,sep="\t")
  rm(mydata)

  print(paste(files[f],"->"))
  print(Sys.time() - ts2)
  rm(ts2)
  rm(resultFilePath)
}

print("Total time:")
print(Sys.time() - ts1)
```

3. Code for uncertainty estimates through OPENBUGS (In R statistical software)

```
getwd()
setwd("C:/Users/nilang/Desktop/DATA")
getwd()

objects()
rm(mydata)
rm(list=objects())

# Load R2WinBUGS package
library(R2OpenBUGS)

# Data (R 'list' format)
I = 30
data = read.table('NW_RAD_SIG_DATA.txt', header = T, sep = '\t')
```

```
attach(data)
summary(data)
datax = list("LAI2200","TLSS","Le","TLSO", "TLSO_W",
"TLSS_W","PVI3","NDVI","SAVI", "DVI", "WDVI")

# MCMC details
nb.iterations = 4000
nb.burnin = 1000

# Initial values

inits<-function(){list (intercept=dnorm(0, 1.0E-3),slope.DVI=dnorm(0, 1.0E-3),
slope.SAVI=dnorm(0, 1.0E-3) ,prec=dgamma(0.001, 0.001))}

nb.chains = 3 #length(inits)

# Parameters to be monitored
parameters <- c("intercept","slope.DVI", "slope.SAVI")

# MCMC simulations
    data.sim <- bugs(datax,
            inits,
            parameters,
            "RAD_R_TLSS_E.txt",
            n.chains = nb.chains,
            n.iter = nb.iterations,
            n.burnin = nb.burnin,
            n.thin = 3,
            debug=TRUE)


# Check convergence
  plot(data.sim, digits.summary=3)
  print(data.sim, digits.summary=3)

# Plot the posterior of beta
  samples <- data.sim$sims.matrix #samples is a matrix with all the MCMC samples. Each
variable is a column

#hist(samples[,3],main='Intercept') #the third column is beta

par(mfrow=c(1,3), mar=c(2,3,2,0.5), mar=c(4.1,3.9,1.1,1.1), oma=c(0,0,0,0), cex=0.75)

plot(density(as.matrix(samples[,1])), xlim = c(-0.005, 5),type = "l", col = "black", main = "",
xlab = "Intercept", ylab = "Probability Density")
```

```
plot(density(as.matrix(samples[,2])), xlim = c(-0.005, 5),type = "l", col = "black", main = "",
xlab = "slope.DVI", ylab = "")
plot(density(as.matrix(samples[,2])), xlim = c(-0.005, 5),type = "l", col = "black", main = "",
xlab = "slope.SAVI", ylab = "")

# Mode of data
x =(as.matrix(samples[,2]))
y = x[rev(order(table(x)))[1]]

summary(samples)
# intercept
quantile(samples[,1], c(.40, .45, .50, .55, .60))
#slope.DVI
quantile(samples[,2], c(.40, .45, .50, .55, .60))
#slope.SAVI
quantile(samples[,3], c(.40, .45, .50, .55, .60))

# Save results
save(data.sim, file = "C:/Users/nilang/Desktop/DATA/para_TLSS_W")
write.table(samples , "C:/Users/nilang/Desktop/DATA/TLSS_W_fit.txt",row.names = F, sep='\t')

myfit <- lm(data$TLSS_W ~ data$DVI + data$SAVI  ,  data=data)
summary(myfit)

coefficients(myfit)
confint(myfit, level=0.95)
Predicted <- fitted(myfit)
summary(Predicted)
fitted(myfit)
Residual<-residuals(myfit)
summary(Residual)
residuals(myfit)
NEW <- cbind(TLSS_W,Predicted, Residual)
write.table(NEW , "C:/Users/nilang/Desktop/DATA/p_TLSS_W.txt", row.names = F,sep='\t')

plot(TLSS_W, residuals(myfit))
abline(a = NULL, b = NULL, h = 0, v = NULL, reg = NULL,coef = NULL, untf = FALSE)
plot(fitted(myfit), residuals(myfit))
abline(a = NULL, b = NULL, h = 0, v = NULL, reg = NULL,coef = NULL, untf = FALSE)

data = read.table('p_TLSO_W.txt', header = T, sep = '\t')
attach(data)
summary(data)

sim<- data$Predicted
obs<- data$TLSS_W
```

```
rmse = sqrt( mean( (sim - obs)^2, na.rm = TRUE) )
rmse
```

4. Code for uncertainty estimates through Bayesian inference and MCMC simulation (In OPENBUGS software)

```
model

        {
            for( i in 1 : N )
              {
                TLSS_E[i] ~ dnorm(mu[i],tau)
mu[i] <- intercept  + slope.DVI * DVI[i]  + slope.SAVI * SAVI[i]
                }


            # Priors for regression parameters
        intercept ~ dnorm(0,0.001)
            slope.DVI ~ dnorm(0,0.001)
            slope.SAVI ~ dnorm(0,0.001)

            #prior for the precision
            tau ~ dgamma(0.001, 0.001)

            sigma <- 1 / sqrt(tau)
   }

    #data
    list(N=30,TLSS_E=c(5.81,8.09,6.26,5.74,6.42,7.72,5.19,7.9,7.46,5.92,6.88,4.07,5.59,6.2,5.8,6.87,5.94,9.23,4.98,7.08,5.85,7.06,4.57,4.96,5.85,5.64,7.53,7.99,7.37,3.69),DVI=c(175.2298019,93.51725996,235.4543678,132.5262049,177.2985662,136.2273031,125.551985,255,104.039528,182.9606771,196.3966371,131.0689714,124.2536841,113.0801169,163.4349115,146.5552733,176.2558535,166.2413452,15.05325308,153.0717169,107.8862791,84.65716091,21.55814305,210.3019622,204.0311384,175.2070822,115.3426505,227.9484356,110.647872,0),SAVI=c(239.7937357,240.140154,179.6712111,245.3214433,138.2702592,229.7132279,223.8849386,142.5145443,255,190.6781454,172.2025034,165.4618911,220.2188987,217.5877064,239.9427044,224.0092261,131.9703826,248.3581125,164.9391785,202.6132691,228.1715343,242.4425574,168.6589881,209.4675912,252.1986837,234.95005,231.2390551,144.8874655,253.1198214,0))

    # Initial Values
    list(intercept=0, slope.DVI=0, slope.SAVI=0, tau=0.001)
```